

Supplemental Materials for “The photometric variability of massive stars due to gravity waves excited by core convection”

EVAN H. ANDERS, DANIEL LECOANET, MATTEO CANTIELLO, KEATON J. BURNS, BENJAMIN A. HYATT, EMMA KAUFMAN,
RICHARD H. D. TOWNSEND, BENJAMIN P. BROWN, GEOFFREY M. VASIL, JEFFREY S. OISHI, AND ADAM S. JERMYN

Contents

1	1. MESA Stellar Models	2
2	1.1. Near-ZAMS calculations used in this work	2
3	1.2. Input physics	2
4	2. Dedalus Equations & Simulation Details	3
5	2.1. The fully compressible equations	3
6	2.2. Implemented equation formulation	3
7	2.3. Boundary conditions	4
8	2.4. Nondimensionalization	4
9	2.5. Discretization and timestepping choices	5
10	2.6. Damping layers	5
11	2.7. Constructing the background state from MESA models	6
12	2.8. Table of simulations	8
13	2.9. Dedalus eigenvalue problems	8
14	2.10. Transforms and spectra	9
15	3. The Transfer Function: Connecting Stellar Variability to Convective Driving	10
16	3.1. Eigenvalue expansion	10
17	3.2. Amplitude equation	10
18	3.3. Oscillatory forcing	11
19	3.4. Connecting the wave luminosity and the forcing	12
20	3.4.1. Connecting the wave luminosity to the wave velocity	12
21	3.4.2. Connection between mode velocity and bulk forcing	12
22	3.4.3. Forcing specification used in amplitude equation	14
23	3.5. Formulae for surface perturbations given the wave luminosity	14
24	4. The Wave Luminosity Spectrum in Wave Generation Simulations	16
25	4.1. Wave flux saturation at high Reynolds number	16
26	4.2. Wave fluxes of different stars	17
27	5. Verification of the Transfer Function in Wave Propagation Simulations	19
28	5.1. Surface perturbations of standing gravity waves	19
29	5.2. Calculation of the transfer function for the Wave Propagation simulation	19
30	5.2.1. Timestepping errors in high-frequency waves	19
31	5.2.2. Comparing Wave Propagation data with transfer function solution	21
32	6. Photometric Variability Spectra	24
33	6.1. GYRE g-modes and MSG surface magnitudes	24
34	6.1.1. Recovering surface magnitude perturbations for each mode with MSG	24
35	6.2. The transfer function	25
36	6.3. Synthesis of photometric variability spectra	26

40	6.4. Red noise fits to synthesized spectra	27
41	7. The Effects of Rotation	30
42	7.1. Observations of stellar rotation and red noise	30
43	7.2. A $15M_{\odot}$ simulation with $P_{\text{rot}} = 10$	31
44	8. Properties of Thermally Damped, Anelastic, Internal Gravity Waves	35
45	8.1. Dispersion and polarization relations	35

46 1. MESA STELLAR MODELS

47 1.1. Near-ZAMS calculations used in this work

48 Our 1D stellar evolution calculations were performed using the Modules for Experiments in Stellar Astrophysics
49 software instrument (Paxton et al. 2011, 2013, 2015, 2018, 2019; Jermyn et al. 2022b, MESA r21.12.1). We evolve
50 stars from the pre-main sequence to a state near the zero-age main sequence (ZAMS) using the `stop_near_zams` flag
51 and setting `Lnuc_div_L_zams_limit = 0.99`. Input mass and metallicity and output surface properties of these ZAMS
52 stars are shown in table 1. Full MESA inlists and the stellar profiles that were used in this work are available online
53 in the Github repository https://github.com/evanhanders/gmode_variability_paper.

54 In section 7 of these supplemental materials, we retrieve stellar luminosity, temperature, and convective timescale
55 data from main sequence models presented in Jermyn et al. (2022a); the models in that paper only extend up to a
56 maximum mass of $60M_{\odot}$, so we additionally run $70 - 120 M_{\odot}$ stellar models using the inlist template from that work.

57 1.2. Input physics

58 The MESA EOS is a blend of the OPAL (Rogers & Nayfonov 2002), SCVH (Saumon et al. 1995), FreeEOS (Irwin
59 2004), HELM (Timmes & Swesty 2000), PC (Potekhin & Chabrier 2010), and Skye (Jermyn et al. 2021) EOSes.

60 Radiative opacities are primarily from OPAL (Iglesias & Rogers 1993, 1996), with low-temperature data from
61 Ferguson et al. (2005) and the high-temperature, Compton-scattering dominated regime by Poutanen (2017). Electron
62 conduction opacities are from Cassisi et al. (2007) and Blouin et al. (2020).

63 Nuclear reaction rates are from JINA REACLIB (Cyburt et al. 2010), NACRE (Angulo et al. 1999) and additional
64 tabulated weak reaction rates Fuller et al. (1985); Oda et al. (1994); Langanke & Martínez-Pinedo (2000). Screening
65 is included via the prescription of Chugunov et al. (2007). Thermal neutrino loss rates are from Itoh et al. (1996).

Table 1. Input (mass M , metallicity Z) and output surface properties (stellar radius R_* , luminosity L , effective temperature T_{eff} , surface gravity g and spectroscopic luminosity $\mathcal{L} = T_{\text{eff}}^4/g$). We take $R_{\odot} = 6.957 \times 10^{10}$ cm, $L_{\odot} = 3.828 \times 10^{33}$ erg/s, $g_{\odot} = 2.7 \times 10^4$ cm s $^{-2}$, and $\mathcal{L}_{\odot} = 4.06 \times 10^{10}$ K 4 s 2 /cm.

$M (M_{\odot})$	Z	$R_* (R_{\odot})$	$\log_{10}(L/L_{\odot})$	$\log_{10}(T_{\text{eff}}/\text{K})$	$\log_{10}(g/g_{\odot})$	$\log_{10}(\mathcal{L}/\mathcal{L}_{\odot})$
3	0.014	1.921	1.970	4.112	-0.089	1.492
15	0.006	4.289	4.289	4.517	-0.088	3.111
40	0.014	8.177	5.359	4.645	-0.223	3.755

2. DEDALUS EQUATIONS & SIMULATION DETAILS

2.1. The fully compressible equations

The simulations presented in this work time-evolve the fully compressible Navier-Stokes equations. Written in a standard form, these equations are (Landau & Lifshitz 1987, §15 and §49)

$$\partial_t \rho + \nabla \cdot (\rho \mathbf{u}) = 0, \quad (1)$$

$$\partial_t \mathbf{u} + \mathbf{u} \cdot \nabla \mathbf{u} = -\frac{1}{\rho} \nabla P + \mathbf{g} + \frac{1}{\rho} \nabla \cdot \overline{\mathbf{\Pi}}, \quad (2)$$

$$\partial_t s + \mathbf{u} \cdot \nabla s = \frac{1}{\rho T} (\nabla \cdot (-\mathbf{F}_{\text{rad}}) + \Phi + Q). \quad (3)$$

We close this system of equations by adopting the equation of state of a compositionally-uniform, calorically-perfect ideal gas,

$$P = \frac{R}{\mu} \rho T \quad \text{or} \quad \frac{ds}{c_p} = \frac{1}{\gamma} d \ln P - d \ln \rho = \frac{1}{\gamma} d \ln T - \frac{\gamma - 1}{\gamma} d \ln \rho. \quad (4)$$

In the above equations, \mathbf{u} is the velocity, s is the specific entropy, ρ is the density, P is the pressure, T is the temperature, \mathbf{g} is the gravitational acceleration, F_{rad} is the radiative flux, and Q is any internal heating or cooling terms (e.g., nuclear burning). In the equation of state (Eqn. 4), R is the ideal gas constant, μ is the mean molecular weight, γ is the adiabatic index, and c_p is the specific heat at constant pressure. The viscous stress tensor $\overline{\Pi}$ is defined

$$\Pi_{ij} = 2\rho\nu \left(E_{ij} - \frac{1}{3}\delta_{ij}\nabla \cdot \mathbf{u} \right) \quad (5)$$

where ν is the kinematic viscosity (the viscous diffusivity) and the strain rate tensor is

$$\overline{\mathbf{E}} = \frac{1}{2} (\nabla \mathbf{u} + [\nabla \mathbf{u}]^T). \quad (6)$$

The viscous heating term is

$$\Phi = 2\rho\nu \left[\text{Tr}(\bar{\mathbf{E}} \cdot \bar{\mathbf{E}}) - \frac{1}{3}(\nabla \cdot \mathbf{u})^2 \right] \quad (7)$$

where Tr is the trace operation.

2.2. Implemented equation formulation

Dedalus uses implicit-explicit timestepping techniques, where the linear terms (and thus linear waves) can be timestepped implicitly, while the nonlinear terms can be timestepped explicitly. To take advantage of this, we decompose our thermodynamics into background components (subscript 0) and fluctuating components (subscript 1) as

$$\ln \rho = (\ln \rho)_0 + (\ln \rho)_1, \quad (8)$$

$$s = s_0 + s_1, \quad (9)$$

$$\varpi = \varpi_0 + \varpi_1 + \varpi_2, \quad (10)$$

where we have defined a modified temperature

$$\varpi \equiv \frac{\mathcal{R}}{\mu} T. \quad (11)$$

We assume that the background state is in hydrostatic equilibrium. We evaluate the linear and nonlinear fluctuations ϖ_1 and ϖ_2 from the equation of state,

$$\frac{\varpi_1}{\varpi_0} = \gamma \left(\frac{s_1}{c_p} + \frac{\gamma - 1}{\gamma} [\ln \rho]_1 \right), \quad \text{and} \quad \frac{\varpi_2}{\varpi_0} \equiv \exp \left(\frac{\varpi_1}{\varpi_0} \right) - \left(1 + \frac{\varpi_1}{\varpi_0} \right), \quad (12)$$

so $T_1 = \varpi_1/(\mathcal{R}/\mu)$ and $T_2 = \varpi_2/(\mathcal{R}/\mu)$. Note also that $(\varpi_1/\varpi_0) = \ln T - \ln T_0$. We also define a modified stress tensor $\bar{\sigma} = \overline{\Pi}/(\rho\nu)$.

Under this thermodynamic decomposition, Eqns. 1-3 can be written with the linear terms on the LHS of the equations and the nonlinear terms on the RHS of the equations,

$$\partial_t \ln \rho_1 + \nabla \cdot \mathbf{u} + \mathbf{u} \cdot \nabla [\ln \rho]_0 = -\mathbf{u} \cdot \nabla [\ln \rho]_1 \quad (13)$$

$$\begin{aligned} \partial_t \mathbf{u} + \gamma \varpi_0 \left(\frac{\nabla s_1}{c_p} + \nabla [\ln \rho]_1 \right) + \mathbf{g} \frac{\varpi_1}{\varpi_0} - [\nu(\nabla \cdot \bar{\sigma} + \bar{\sigma} \cdot \nabla (\ln \rho)_0) + \bar{\sigma} \cdot \nabla \nu] + \mathcal{D}(r) \mathbf{u} \\ = -\mathbf{u} \cdot \nabla \mathbf{u} - 2\boldsymbol{\Omega} \times \mathbf{u} - \left[\gamma \varpi' \left(\frac{\nabla s_1}{c_p} + \nabla [\ln \rho]_1 \right) + \mathbf{g} \frac{\varpi_2}{\varpi_0} \right] + \nu \bar{\sigma} \cdot \nabla (\ln \rho)_1, \end{aligned} \quad (14)$$

$$\partial_t s_1 + \mathbf{u} \cdot \nabla s_0 + \left(\frac{1}{\rho_0 T_0} \right) [\nabla \cdot (\mathbf{F}_{\text{rad}})] = -\mathbf{u} \cdot \nabla s_1 + \left(\frac{1}{\rho T} - \frac{1}{\rho_0 T_0} \right) [\nabla \cdot (-\mathbf{F}_{\text{rad}})] + \frac{1}{\rho T} [\Phi + Q] \quad (15)$$

Here, the term with $\mathcal{D}(r)$ is a damping term (see Sect. 2.6), and we study one rotating simulation in Sec. 7, so we include the Coriolis term $2\boldsymbol{\Omega} \times \mathbf{u}$, where $\boldsymbol{\Omega} = \hat{z}(2\pi/P_{\text{rot}})$ and P_{rot} is the rotation period of the star, and we set $\boldsymbol{\Omega} = \mathbf{0}$ for nonrotating runs. As we detail in Sec. 2.7, the heating term Q in Eqn. 15 includes both nuclear burning and the divergence of the radiative flux from the MESA model. As a result, we only solve for the radiative flux associated with the temperature fluctuations around the background state.

We further simplify the radiative flux term by neglecting the fully nonlinear portion of the radiative flux associated with T_2 and only solve for the flux associated with the linear perturbations to the temperature, $\mathbf{F}_{\text{rad}} = -k_{\text{rad}} \nabla T_1 = -k_{\text{rad}} \nabla (\varpi_1 / [\mathcal{R}/\mu])$. The viscous diffusivities and radiative conductivities used in our simulations are specified in Sec. 2.7. The characteristic Mach numbers of convective flows are very low (see Table 3), and we expect linear temperature perturbations of the order $T_1/T_0 \sim \text{Ma}^2 \sim 10^{-6}$ (Anders & Brown 2017), and we expect nonlinear terms to be of order $\text{Ma}^4 \sim 10^{-12}$ per Eqn. 12 (because $\varpi_2/\varpi_0 \approx \mathcal{O}([\varpi_1/\varpi_0]^2)$ after Taylor expanding the exponential), so this term that we neglect is small. Aside from the inclusion of the Coriolis term in a rotating frame and linearizing the radiative flux, Eqns. 13-15 are a mathematically-equivalent restatement of the fully compressible equations Eqns. 1-3.

2.3. Boundary conditions

At the outer boundary $r = R$ of the Dedalus simulation, we impose the following boundary conditions:

$$\hat{e}_r \cdot \nabla \varpi_1(r = R) = 0, \quad \hat{e}_r \cdot \mathbf{u}(r = R) = 0, \quad E_{r,\phi}(r = R) = E_{r,\theta}(r = R) = 0. \quad (16)$$

These conditions make it so that there are no flux, velocity, or angular stress perturbations at the outer boundary of the simulation. We split the simulation into different radial domains, and expand all variables in terms of different basis functions across each radial domain (see Sec. 2.5). At the boundaries of the radial domains, we impose continuity of $\hat{e}_r \cdot \mathbf{u}$, s_1 , $(\ln \rho)_1$, $\hat{e}_r \cdot \nabla (\varpi_1 / \varpi_0)$, $E_{r,\phi}$, and $E_{r,\theta}$. For the $\ell = 0$ mode, instead of specifying that $\hat{e}_r \cdot \nabla \varpi_1(r = R) = 0$, we instead specify that there are no fluctuations in the volume-integrated total system energy $\mathcal{E} = 0.5\rho|u|^2 + \rho\phi + P/(\gamma-1)$; while these are mathematically equivalent conditions, they can in practice produce slightly different solutions due to the accumulation of timestepping errors from e.g., the tau-method enforcement of boundary conditions over many timesteps¹.

2.4. Nondimensionalization

We take the radius of the core convection zone of our star to be our nondimensional unit of length, $L_C = r_{\text{core}}$. We use the density and temperature values at that radial coordinate to set the nondimensional temperature and mass units, $T_C = T(r = r_{\text{core}}) \& m_C = \rho(r_{\text{core}}) L_C^3$. We use the maximum value of the buoyancy frequency in our simulation domain to determine the nondimensional time unit, $\tau_{\text{nd}} = (2\pi)/\max(N)$. From these four fundamental units, all other quantities (energy, entropy, etc.) can be constructed.

We find that convective dynamics occur on a timescale which is related to the nuclear burning rate in the core, $\tau_{\text{heat}} = [\epsilon(r = 0)/L_C^2]^{-1/3}$, where ϵ is the energy generation rate in $\text{erg g}^{-1} \text{s}^{-1}$, and we evolve our simulations for tens to hundreds of heating timescales. We refer the reader to Table 2 for key nondimensional values.

¹ We find that enforcing energy conservation in this way introduces a small stochastic forcing into $\ell = 0$ sound waves. There are no $\ell = 0$ gravity waves (see the dispersion relation, Sec. 8), so we do not analyze the $\ell = 0$ motions in this paper. We have verified that using a standard gradient boundary condition for $\ell = 0$ (e.g., $\hat{e}_r \cdot \nabla \varpi_1 = 0$) does not affect the power of gravity waves.

Table 2. Input (mass M , metallicity Z) parameters of the MESA models and associated nondimensional quantities used in Wave Generation (WG) and Wave Propagation (WP) Dedalus simulations, as well as the characteristic heating timescale, the MLT velocity, and the value of the specific heat at constant pressure (c_p) and adiabatic index (γ) used in the simulation.

$M (M_\odot)$	Z	Sim. Type	L_C (cm)	m_C (g)	T_C (K)	τ_{nd} (s)	τ_{heat} (s)	$\langle u_{\text{MLT}} \rangle$ (cm s $^{-1}$)	c_p (erg g $^{-1}$ K $^{-1}$)	γ
3	0.014	WG	1.87×10^{10}	1.93×10^{32}	1.89×10^7	3.25×10^3	5.74×10^5	1.37×10^4	3.49×10^8	1.654
15	0.006	WG	8.21×10^{10}	1.89×10^{33}	2.35×10^7	8.41×10^3	4.66×10^5	6.68×10^4	3.88×10^8	1.560
15	0.006	WP	8.21×10^{10}	1.89×10^{33}	2.35×10^7	6.09×10^3	4.66×10^5	6.68×10^4	3.88×10^8	1.560
40	0.014	WG	2.06×10^{11}	6.01×10^{33}	2.11×10^7	1.52×10^4	5.55×10^5	1.33×10^5	4.20×10^8	1.481

2.5. Discretization and timestepping choices

We solve Eqns. 13-15 along with the boundary conditions in Section 2.3 using version 3 of the Dedalus pseudospectral framework (Burns et al. 2020). Simulations scripts can be found in the `gmode_variability_paper`² Github repository; these scripts rely on the separate `compressible_stars`³ Github repository and were run using the `master` branch of the `Dedalus` Github repository⁴ at the commit with short-sha `29f3a59`. The simulation domain is decomposed into a `BallBasis` (with nr_B radial coefficients) and then either one (for Wave Generation simulations) or two (for the Wave Propagation simulation) `ShellBasis` objects (with nr_{s1} , nr_{s2} radial coefficients). In the main text, the “number of resolution elements across the convective core” is $2nr_B$, which is the number of elements across the *diameter* of the `BallBasis` for comparison with “star in a box” simulations performed in Cartesian domains. The `BallBasis` expands variables using a basis of radially-weighted Zernike polynomials (Vasil et al. (2019), though see section 6.1.2 of Lecoanet et al. (2019) for subtleties of resolution) and the `ShellBasis` expands variables radially using a Chebyshev polynomial basis. The `BallBasis` radially spans $r \in [0, 1.1]$ in nondimensional units. In Wave Generation simulations, the `ShellBasis` spans $r \in [1.1, 2]$, and for Wave Propagation simulations, the two `ShellBasis` domains respectively span $r \in [1.1, 2.98]$ and $r \in [2.98, 3.38]$. Variables are expanded angularly over azimuth $\phi \in [0, 2\pi]$ and colatitude $\theta \in [0, \pi]$ using spin-weighted spherical harmonics with maximum harmonic degree L_{max} and angular wavenumbers $m \in [-L_{\text{max}}, L_{\text{max}}]$.

Initial value problems (“simulations”) use the time-stepper SBDF2 (Wang & Ruuth 2008) with a CFL safety factor of 0.2. For each background state, we initialize a high-diffusivity simulation using noise in the entropy field of order 10^{-8} . To achieve more turbulent simulations, we “bootstrap” simulations by using the nonlinear dynamical state of a lower resolution simulation as initial conditions and increasing the resolution while decreasing the diffusivity. This bootstrapping technique avoids the transient associated with the onset of the convective instability from a stationary state.

Spectral methods with finite coefficient expansions cannot capture true discontinuities. To approximate discontinuous functions, we define a smooth Heaviside step function centered at $r = r_0$,

$$H(r; r_0, d_w) = \frac{1}{2} \left(1 + \text{erf} \left[\frac{r - r_0}{d_w} \right] \right). \quad (17)$$

where erf is the error function and d_w determines the width of the smooth transition.

2.6. Damping layers

Wave Generation simulations include a damping layer in Eqn. 14 of the form,

$$\mathcal{D}(r) = \tau_D^{-1} [1 - H(r; 1.85, 0.07)], \quad (18)$$

which introduces a Newtonian damping to the velocity field in the outer $\sim 15\text{-}20\%$ of the radiative zone, similar to the damping layer introduced by Couston et al. (2018) and Lecoanet et al. (2021). In Wave Generation simulations, we take $\tau_D^{-1} = \tau_{\text{nd}}^{-1}$, the timescale associated with the maximum buoyancy frequency in the simulation domain. In Wave Propagation simulations, we set $\mathcal{D}(r) = 0$.

² https://github.com/evanhanders/gmode_variability_paper

³ https://github.com/evanhanders/compressible_stars

⁴ <https://github.com/DedalusProject/dedalus>

161 2.7. Constructing the background state from MESA models

162 The background state in our simulations ($(\ln \rho)_0, s_0, \varpi_0, \mathbf{g}, Q, \gamma$, and c_p , and k_{rad}) are constructed using information
 163 from MESA model stellar models. We take the value of γ and c_p to be constant and set them to their values at $r = 0$
 164 in the MESA model. To construct the radial stratification, we do the following.

165 In the **BallBasis**, $r \leq 1.1$, it is crucial for the background fields to satisfy the regularity of the polynomial basis
 166 as $r \rightarrow 0$. To begin constructing our simulation structure, we fit a quadratic polynomial $\tilde{N}^2 = A + Br^2$ such that
 167 $\tilde{N}^2(r = 1.1) = N_{\text{MESA}}^2(r = 1.1)$ and $\nabla \tilde{N}^2(r = 1.1) = \nabla N_{\text{MESA}}^2(r = 1.1)$, and we construct the simulation N^2 profile as

$$168 \quad N_{\text{sim}}^2 = \begin{cases} H(r; 1.07, 0.03)\tilde{N}^2 & r \leq 1.1 \\ N_{\text{MESA}}^2 & r > 1.1 \end{cases}, \quad (19)$$

169 where H is defined in Eqn. 17. We next define the convective luminosity in the simulation to be

$$170 \quad L_{\text{conv,sim}} = [1 - H(r; 0.9, 0.05)][1 - H(r; 0.95, 0.05)]L_{\text{conv,MESA}}, \quad (20)$$

171 so that it smoothly transitions to zero. The convective luminosity that MESA outputs is discontinuous at the outer
 172 edge of the convective core (at $r = 1$). We make use of two broad heaviside windows at $r = 0.9$ and $r = 0.95$ so that
 173 L_{conv} gradually transitions to zero within floating point accuracy when we construct our simulation background. We
 174 then solve for the simulation heating term by evaluating

$$175 \quad \mathcal{Q}_{\text{sim}} = [1 - H(r; 1.045, 0.033)]\nabla \cdot \left(\frac{L_{\text{conv,sim}}}{4\pi r^2} \hat{e}_r \right), \quad (21)$$

176 where we include the $(1 - H)$ term to ensure that \mathcal{Q}_{sim} is zero to within floating point precision at the interface
 177 between different spectral bases at $r = 1.1$. Note that since \mathcal{Q}_{sim} is based on the divergence of the *convective* flux
 178 rather than the total stellar flux or luminosity, it is encoded both with heating information from nuclear reactions and
 179 cooling information associated with changing radiative luminosity.

180 We set the simulation density profile $\ln \rho_{0,\text{sim}} = \ln \rho_{\text{MESA}}$. We construct a hydrostatically-equilibrated background
 181 state with the specified N_{sim}^2 and $\ln \rho_{0,\text{sim}}$ by using **Dedalus** to solve the following boundary value problem for s_0 and
 182 ϖ_0 on our spectral bases,

$$183 \quad \nabla \ln \rho_{0,\text{sim}} \cdot \nabla \left(\frac{s_{0,\text{sim}}}{c_p} \right) = -\frac{N_{\text{sim}}^2}{\gamma \varpi_{0,\text{sim}}} - \frac{|\nabla s_{0,\text{sim}}|^2}{c_p^2}, \quad \text{with } \varpi_0 = \frac{\mathcal{R}}{\mu} \exp \left(\gamma \left[\frac{s_{0,\text{sim}}}{c_p} + \frac{\gamma - 1}{\gamma} \ln \rho_{0,\text{sim}} \right] \right), \quad (22)$$

184 under the boundary conditions that $\ln(\varpi_{0,\text{sim}})(r = 1) = 0$ and $s_{0,\text{sim}}$ is continuous at the interfaces of different spectral
 185 bases. Once we know the thermal stratification, we solve for the gravitational potential, ϕ ,

$$186 \quad \nabla \phi_{\text{sim}} - \gamma \varpi_{0,\text{sim}} \left(\frac{\nabla s_{0,\text{sim}}}{c_p} + \nabla \ln \rho_{0,\text{sim}} \right) = 0 \quad (23)$$

187 while specifying that $\phi_{\text{sim}}(r = R) = 0$ (where R is the outermost radial coordinate of the simulation domain), and
 188 ϕ_{sim} is continuous at the interfaces of different spectral bases. Eqn. 22 solves for the hydrostatically equilibrated s_0
 189 that is consistent with our equation of state (Eqn. 4) under the constraints of the specified N^2 and $\ln \rho_0$ profiles by
 190 taking a dot product between $\nabla s_0/c_p$ and a rearranged Eqn. 23.

191 We specify the viscous diffusivity ν_{sim} present in our simulations to control the degree of turbulence. To construct
 192 the radiative diffusivity profile used in our simulations, we set $\chi_{\text{rad}} = \nu_{\text{sim}} + \chi_{\text{MESA}}$ where $\chi_{\text{MESA}} = 16\sigma_{\text{SB}}T^3/(3\rho^2 c_p \kappa)$,
 193 where σ_{SB} is the Stefan-Boltzmann constant, and κ is the opacity. We then use this radial profile to construct the
 194 simulation radiative conductivity $k_{\text{rad}} = \rho_{\text{sim}} c_p \chi_{\text{rad}}$. In the convective core, ν_{sim} is larger than the viscous diffusivity
 195 and radiative diffusivity present in the MESA model. In the outer envelope of our $15 M_{\odot}$ Wave Propagation simulation,
 196 the radiative diffusivity in the simulation and MESA model become larger than ν_{sim} (see Fig. 1). The Prandtl number
 197 $\text{Pr} = \nu/\chi_{\text{rad}} = 1$ in the convection zone and $\text{Pr} < 1$ near the surface of the Wave Propagation simulation.

198 We expand each necessary background variable in terms of our spectral bases then truncate those expansions using
 199 a maximum specified number of spectral coefficients; we truncate the expansions to increase the sparsity of our solver
 200 matrices and decrease memory costs of our simulations. We use 60 coefficient terms in the **BallBasis** for all profiles

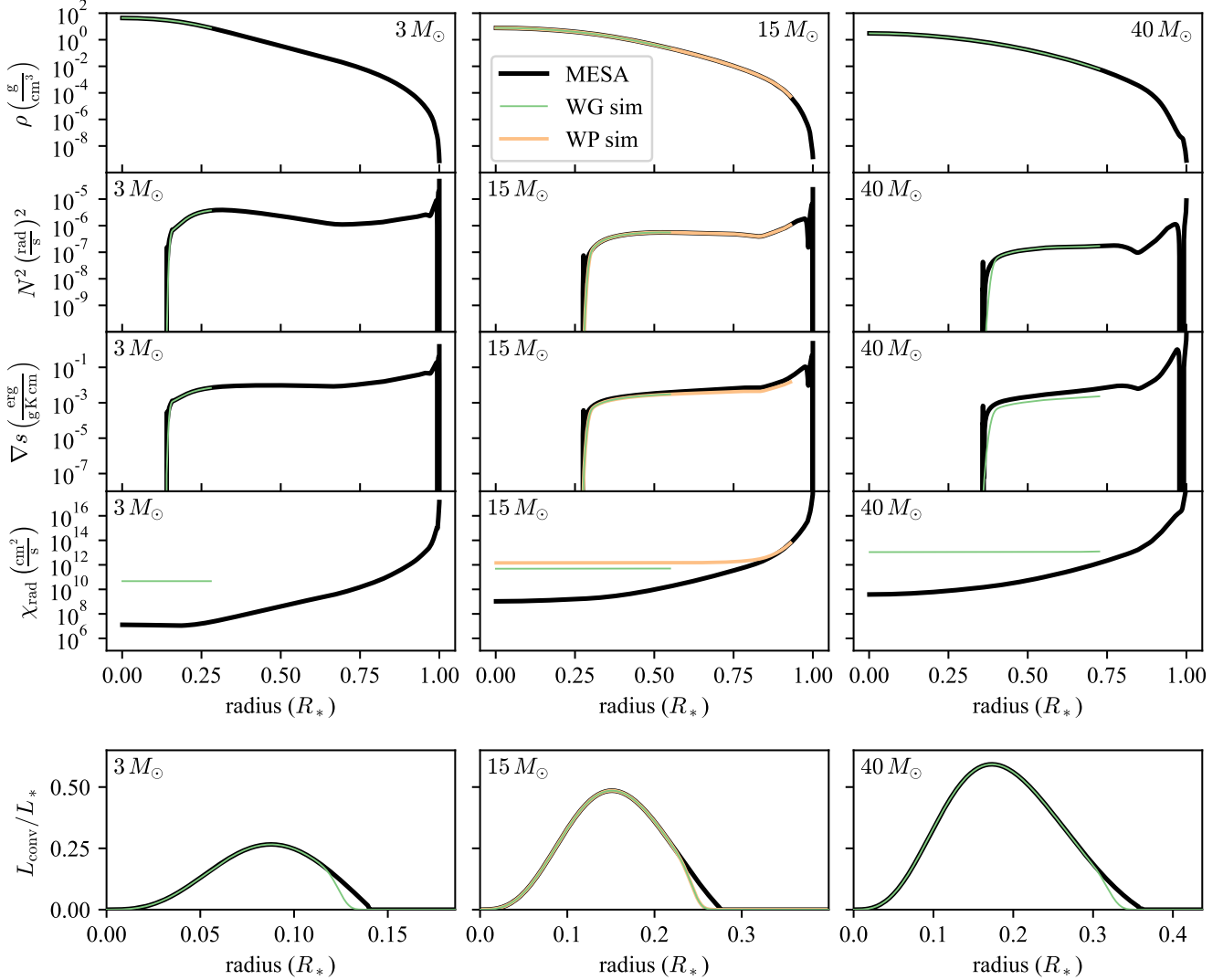


Figure 1. Radial profiles of various quantities from MESA stellar models are shown in black for the $3 M_{\odot}$ (left), $15 M_{\odot}$ (middle), and $40 M_{\odot}$ (right) stars; these profiles are compared to Wave Generation simulations (WG, green) and the Wave Propagation simulation (WP, peach). We show the density ρ (top row), the square of the Brunt-Väisälä frequency (second row), the specific entropy gradient (third row), and the radiative diffusivity (fourth row). In the bottom row, we zoom in the x-axis on the core convection zone and show the convective luminosity.

except for k_{rad} where we use 32 and ∇s_0 where we use 90. The Wave Propagation simulations respectively uses 42 and 36 radial coefficients to expand all profiles in the two `ShellBasis` expansions, except for k_{rad} which respectively uses 32 and 5. The Wave Generation simulation uses 40 radial coefficients in the `ShellBasis` for all profiles, except for k_{rad} and ∇s_0 which each use 30. After expansion and truncation, we multiply the expanded ∇s_0 field by $H(r, 0.95, 0.03)$ to make ∇s_0 as close to zero as possible in the bulk convection zone. Finally, we ensure that our simulations are in perfect energetic equilibrium by subtracting the small volume-averaged value of \mathcal{Q}_{sim} from the heating profile,

$$Q_{\text{sim}} = \mathcal{Q}_{\text{sim}} - \frac{\int \mathcal{Q}_{\text{sim}} dV}{\int dV}, \quad (24)$$

where Q_{sim} is the true heating profile used in our simulations.

Comparisons between profiles of ρ , N^2 , ∇s , χ_{rad} , and the convective luminosity L_{conv} in the MESA model and our Dedalus simulations are shown in Fig. 1. Full MESA profiles are shown as black lines, while Wave Generation (WG) simulations are shown as green lines and our Wave Propagation (WP) simulation is shown as a peach colored line. As expected, our ρ and N^2 profiles faithfully reproduce the MESA model, except right above the core convection zone

Table 3. Input and basic output values from the various Dedalus simulations used in this work. Columns show the star model mass, simulation type (WP - Wave Propagation or WG - Wave Generation), the number of spherical harmonic degrees used (including $\ell = 0$), the number of coefficients in the radial coefficient expansion ($\{\text{nr}_B, \text{nr}_{s1}, \text{nr}_{s2}\}$ for WP, $\{\text{nr}_B, \text{nr}_{s1}\}$ for WG), the viscous diffusivity in the simulation, the stellar rotation period in days, the simulation run time in heating timescales, and the core-average of the velocity, Mach number, and Reynolds number ($\text{Re} = \langle u \rangle_{\text{core}} L_C / \nu_{\text{sim}}$). The heating timescales are shown in table 2.

Model Star	Sim. Type	$L_{\max} + 1$	$N_{\max} + 1$	$\nu_{\text{sim}} (\text{cm}^2 \text{s}^{-1})$	$P_{\text{rot}} (\text{d})$	$t_{\text{sim}} (t_{\text{heat}})$	$\langle u \rangle_{\text{core}} (\text{cm s}^{-1})$	$\langle \text{Ma} \rangle_{\text{core}}$	$\langle \text{Re} \rangle_{\text{core}}$
15	WP	256	{256,192,64}	1.44×10^{12}	∞	324	5.77×10^4	9.17×10^{-4}	3.28×10^3
15	WG	512	{512,192}	4.81×10^{11}	∞	39	5.85×10^4	9.29×10^{-4}	9.97×10^3
15	WG	384	{384,192}	7.22×10^{11}	∞	43	5.84×10^4	9.29×10^{-4}	6.64×10^3
15	WG	256	{256,128}	1.44×10^{12}	∞	100	5.72×10^4	9.08×10^{-4}	3.25×10^3
15	WG	256	{256,128}	1.44×10^{12}	10	120	7.94×10^4	1.26×10^{-3}	4.51×10^3
15	WG	128	{128,96}	3.60×10^{12}	∞	100	5.40×10^4	8.57×10^{-4}	1.23×10^3
15	WG	128	{128,96}	7.22×10^{12}	∞	100	5.05×10^4	8.01×10^{-4}	5.74×10^2
15	WG	96	{96,64}	1.44×10^{13}	∞	100	4.62×10^4	7.32×10^{-4}	2.63×10^2
3	WG	256	{256,128}	4.69×10^{10}	∞	50	9.00×10^3	1.68×10^{-4}	3.04×10^3
40	WG	256	{256,128}	9.83×10^{12}	∞	35	1.31×10^5	2.10×10^{-3}	2.47×10^3

where we intentionally smooth the MESA profile (Eqn. 19). In the $3 M_{\odot}$ star, ∇s also faithfully reproduces the MESA model, but for higher mass stars there is a slight disagreement between the MESA and Dedalus ∇s profiles. This occurs because our simple equation of state (Eqn. 4) does not capture radiation pressure which becomes important in higher mass stars, and it should be included in future studies of the highest mass stars. L_{conv} reproduces the stellar convective luminosity, except at the outside of the convection zone where we explicitly smoothed the heating profile.

2.8. Table of simulations

Resolution and input characteristics and key output quantities from the simulations conducted in this work are shown in Table 3. The $15 M_{\odot}$ model is our fiducial model. The two simulations displayed in Fig. 1 of the main text are the $15 M_{\odot}$ WP simulation and the highest-resolution $15 M_{\odot}$ WG simulation ($L_{\max} + 1 = 512$). The predictions presented in Fig. 2 of the main text use the Wave Luminosity measured from the three WG simulations with $L_{\max+1} = 256$ for the 3, 15, and $40 M_{\odot}$ models.

2.9. Dedalus eigenvalue problems

To obtain the eigenvalues and eigenfunctions associated with gravity waves in our **Dedalus** simulation domain, we perform a numerical eigenvalue solve. We set the nonlinear right-hand side terms of Eqns. 13–15 to zero and we solve for the eigenvalues using a domain with the same radial resolution as our nonlinear simulations. For each spherical harmonic degree ℓ , we perform a dense eigenvalue solve with $m = 0$ and receive a set of eigenvalues of the form $\omega_n = \omega_{0,n} - i\gamma_n$, where $\omega_{0,n}$ and γ_n are real numbers corresponding to the oscillation angular frequency and damping rate of the mode. For each eigenmode, we calculate the integrated kinetic energy of the mode $K(r = r') = 4\pi \int_0^{r'} (\rho_0 \mathbf{u}^* \cdot \mathbf{u}) r^2 dr$ with $K(r = 1)$ being the kinetic energy in the core convection zone and $K(r = R)$ being the total mode energy. In addition to real solutions, numerical eigenvalue solves return many spurious eigenvalues (Boyd 2001, Ch. 7). We filter out spurious eigenvalues/eigenmodes in a manner similar to `eigentools` (Oishi et al. 2021) as follows:

1. Only keep finite eigenvalues.
2. Only keep eigenvalues with positive real components⁵, $\omega_{0,n} > 0$.
3. Only keep g-modes and filter out p-modes. This means that there must be at least one radial coordinate where both $\omega_{0,n} < S_{\ell}$ the Lamb frequency and $\omega_{0,n} < N$ the buoyancy frequency.

⁵ For each mode, there is a complementary mode with $\omega_{0,n} < 0$ and the same γ_n that we are discarding. These complementary modes have the same eigenvectors as the modes that we keep, and lead to poorly conditioned systems in our normal mode expansion (Sec. 3) if they are not discarded.

- 238 4. Discard purely damped eigenvalues where $|\omega_{0,n}/\gamma_n| \leq 10^{-4}$.
- 239 5. Discard any growing modes $\gamma_n > 0$.
- 240 6. Discard any modes for which more than 50% of the kinetic energy is located in the CZ, $K(r=1)/K(r=R) > 0.5$.
- 241 7. Discard any modes for which less than one part in 10^{12} of the kinetic energy is located in the CZ, $K(r=1)/K(r=R) < 10^{-12}$; these are spurious modes without evanescent tails.

243 We then sort the eigenvalues by $\omega_{0,n}$, descending (the highest frequency, least damped wave comes first). For each
 244 remaining eigenvalue, we perform a sparse solve around ω_n with the radial coefficient resolution increased by a factor
 245 of 3/2. After the sparse solve, we keep eigenvalues ω_m from the high-resolution solve when:

- 246 1. The high-resolution eigenvalue is the same as the low-resolution eigenvalue within a tolerance, $|\omega_m - \omega_n|/|\omega_n| < c$
 247 with $c = 10^{-4}$.
- 248 2. The integrated kinetic energy $K(r=R)$ differs by no more than a factor of \sqrt{c} between the high-resolution and
 249 low-resolution solves.

250 The set of remaining eigenvalues ω_n is taken to be the complete set of solutions. We normalize the eigenfunctions by
 251 the value where the radial velocity eigenfunction's absolute value is maximized before performing any other operation.

252 2.10. Transforms and spectra

253 All wave flux and power spectra in this work are calculated from long time series of data of our state variables
 254 projected onto a 2D sphere. Given a 3D data cube of a variable $a(t, \phi, \theta)$, we transform the data into frequency space
 255 as

$$256 a(t, \phi, \theta) \xrightarrow{\text{SHT}} a_{\ell,m}(t) \xrightarrow{\text{FT}} \hat{a}_{\ell,m}(f). \quad (25)$$

257 We perform the spherical harmonic transform (SHT) using Dedalus. Dedalus returns two coefficient amplitudes, b_1
 258 and b_2 , corresponding to the $\cos(m\phi)$ and $-\sin(m\phi)$ components. From these, we construct the spherical harmonic
 259 amplitude $a_{\ell,m}(t) = b_1 + ib_2$.

260 We calculate the Discrete Fourier Transform using NumPy and define its normalization such that

$$261 \hat{a}_{\ell,m,f} = \frac{1}{N} \sqrt{\frac{8}{3}} \sum_{j=0}^{N-1} H_N(j) \hat{a}_{\ell,m}(t_j) \exp \left\{ -2\pi i \frac{jf}{N} \right\} \quad (26)$$

262 In this definition, $H_N(j)$ is the j th point of the Hanning window defined over N total data points, and the factor of
 263 $\sqrt{8/3}$ accounts for this window.

264 To calculate a power-like quantity (power spectrum, wave flux spectrum), we multiply one transformed field with
 265 the complex conjugate of another, e.g., $P_A(f) = \hat{a}^* \hat{a}$. To properly account for power in negative frequencies, we define
 266 $P_A(f) = P_A(f) + P_A(-f)$ for all $f \geq 0$.

267 To calculate the wave luminosity, we output in real space the enthalpy $H = \rho h = (c_p \mu / \mathcal{R}) P$ and radial velocity
 268 $u_r = \mathbf{u} \cdot \hat{\mathbf{e}}_r$. We take transforms per the above recipe and calculate the wave luminosity $L_w(f, \ell) = 4\pi R^2 \hat{H}^* \hat{u}_r$, where
 269 R is the radial coordinate of the shell where the fields are sampled. In our wave propagation simulation, we compare
 270 the transfer function to the entropy amplitude; to calculate the entropy amplitude we output s_1 at the outer boundary
 271 of the simulation, then calculate $|s_1|(f, \ell) = \sqrt{\hat{s}_1^* \hat{s}_1}$.

272 Data used to verify the transfer function and measure the wave luminosity are recorded at 30 min. intervals, which
 273 match the observational “long-cadence” observing mode of the K2 (Howell et al. 2014) and TESS (Ricker et al. 2014)
 274 satellites.

275 3. THE TRANSFER FUNCTION: CONNECTING STELLAR VARIABILITY TO CONVECTIVE DRIVING

276 In the following, we derive the transfer function which connects the wave luminosity to perturbations at the stellar
 277 surface. Sections 3.1, 3.2, and 3.4.2 closely follow appendices A and B of Lecoanet et al. (2019); we reproduce these
 278 derivations here so that the reader may appreciate the differences in derivation that come in sections 3.3, 3.4.1, and
 279 3.5.

280 3.1. *Eigenvalue expansion*

281 We assume that the gravity waves which propagate in the envelope of a star or in the radiative zone of our simulation
 282 can be described by a set of eigenvalues ω_n and corresponding eigenfunctions describing perturbations to e.g., the
 283 velocity and the photometric variability. We assume that the radial and temporal evolution of the system variables at
 284 each harmonic degree ℓ can be described by an expansion of the eigenfunctions,

$$\mathbf{u}_\ell(r, t) = \sum_n A_\ell(t; \omega_n) \widetilde{\mathbf{u}}_{\ell,n}(r; \omega_n) \exp(-i\omega_n t), \quad (27)$$

$$\Delta m_\ell(R_*, t) = \sum_n A_\ell(t; \omega_n) \widetilde{\Delta m}_{\ell,n}(R_*; \omega_n) \exp(-i\omega_n t), \quad (28)$$

288 where the eigenfunctions are denoted by tildes, and $A_\ell(t; \omega_n)$ is the time-dependent amplitude of the wave with
 289 eigenvalue ω_n . Here, \mathbf{u}_ℓ and Δm_ℓ are respectively the velocity and photometric magnitude fluctuations at spherical
 290 harmonic degree ℓ . In other words, given the eigenfunctions and an expression for the wave amplitudes $A_\ell(t; \omega_n)$, we
 291 can determine the full state of the system, including the surface brightness perturbations. Note that Eqns. 27 and 28
 292 do not include any angular dependence; the full system state is obtained by multiplying by the spherical harmonics
 293 Y_ℓ^m and summing over ℓ ,

$$\mathbf{u}(r, \theta, \phi, t) = \sum_\ell \widetilde{\mathbf{u}}_\ell(r, t) Y_\ell^m(\theta, \phi), \quad (29)$$

$$\Delta m(R_*, \theta, \phi, t) = \sum_\ell \widetilde{\Delta m}_\ell(R_*, t) Y_\ell^m(\theta, \phi). \quad (30)$$

297 In this work we will define the inner product,

$$\langle \mathbf{f}, \mathbf{g} \rangle \equiv \int_{\mathcal{V}} \rho_0 \mathbf{f}^* \cdot \mathbf{g} d\mathcal{V}, \quad (31)$$

299 where \mathcal{V} is the full volume of our spherical domain, $d\mathcal{V}$ is the volume element, and \mathbf{f}^* is the complex-conjugate of the
 300 vector \mathbf{f} . We will find it useful to use the velocity eigenfunctions to define a dual basis $\widetilde{\mathbf{u}}_\ell^\dagger$ which satisfies

$$\langle \widetilde{\mathbf{u}}_\ell^\dagger(\omega_j), \widetilde{\mathbf{u}}_\ell(\omega_k) \rangle = \delta_{\omega_j, \omega_k}. \quad (32)$$

302 3.2. *Amplitude equation*

303 To find A_ℓ , we assume that the evolution equation for the wave velocity at each ℓ and angular frequency ω can be
 304 can be written

$$\partial_t \mathbf{u}_\ell(\mathbf{r}, t) = \mathcal{L}(\mathbf{u}_\ell) + \mathbf{F}_\ell(\mathbf{r}, t; \omega), \quad (33)$$

306 where \mathcal{L} is the linear operator which encompasses all of the terms describing wave motion and \mathbf{F} is the nonlinear wave
 307 forcing at ω . We now expand the velocity in Eqn. 33 using Eqn. 27 and project out the individual modes by taking
 308 an inner product of the dual basis $\widetilde{\mathbf{u}}_\ell^\dagger(\omega_n)$ and Eqn. 33,

$$\partial_t [A_\ell(t; \omega_n) \exp(-i\omega_n t)] = -i\omega_n A_\ell(t; \omega_n) \exp(-i\omega_n t) + \langle \widetilde{\mathbf{u}}_\ell^\dagger(\omega_n), \mathbf{F}(\mathbf{r}, t; \omega) \rangle, \quad (34)$$

310 This corresponds to Eqn. 14 in appendix A of Lecoanet et al. (2019). We apply the multiplication rule to the time
 311 derivative and find that one of its terms cancels out the term from \mathcal{L} . Multiplying the equation by $\exp(i\omega_n t)$, we find

$$\partial_t A_\ell(t; \omega_n) = \exp(i\omega_n t) \langle \widetilde{\mathbf{u}}_\ell^\dagger(\omega_n), \mathbf{F}(\omega) \rangle. \quad (35)$$

313 Integrating from 0 to t with the boundary condition $A_\ell(t=0; \omega_n) = 0$, we get a general expression for the amplitude,

$$A_\ell(t; \omega_n) = \int_0^t dt \exp(i\omega_n t) \langle \widetilde{\mathbf{u}}_\ell^\dagger(\omega_n), \mathbf{F}(\omega) \rangle. \quad (36)$$

315 3.3. *Oscillatory forcing*

To move forward from Eqn. 36, we must specify something about the forcing term $\mathbf{F}(\omega)$. We will assume that the forcing \mathbf{F} is separable in space and time, that it is purely in the angular direction and zero in the radial direction, and that the temporal component is oscillatory with frequency ω with phase ϕ ,

$$319 \quad \mathbf{F}_\ell(\mathbf{r}, t; \omega) = (0, \zeta(\mathbf{r}) \sin(\omega t + \phi)), \quad (37)$$

so that Eqn. 36 becomes

$$321 \quad A_\ell(t; \omega_n) = \langle \tilde{\mathbf{u}}_{\ell,h}^\dagger(\omega_n), \zeta(\mathbf{r}) \rangle \int dt \exp(i\omega_n t) \sin(\omega t + \phi) = \langle \tilde{\mathbf{u}}_{\ell,h}^\dagger(\omega_n), \zeta(\mathbf{r}) \rangle \exp(i\omega_n t) \frac{\omega \cos(\omega t + \phi) - i\omega_n \sin(\omega t + \phi)}{(\omega_n - \omega)(\omega_n + \omega)} + C. \quad (38)$$

Here $\tilde{\mathbf{u}}_{\ell,h}$ is the horizontal (angular) component of the eigenvector $\tilde{\mathbf{u}}_\ell$. Integrating in time, we find

$$323 \quad A_\ell(t; \omega_n) = \frac{\langle \tilde{\mathbf{u}}_{\ell,h}^\dagger(\omega_n), \zeta(\mathbf{r}) \rangle}{(\omega_n - \omega)(\omega_n + \omega)} [\exp(i\omega_n t) (\omega \cos(\omega t + \phi) - i\omega_n \sin(\omega t + \phi)) - (\omega \cos(\phi) - i\omega_n \sin(\phi))]. \quad (39)$$

Substitution into Eqn. 27 gives

$$324 \quad \mathbf{u}_\ell(r, t) = \sum_n \tilde{\mathbf{u}}_\ell(r; \omega_n) \frac{\langle \tilde{\mathbf{u}}_{\ell,h}^\dagger(\omega_n), \zeta(\mathbf{r}) \rangle}{(\omega_n - \omega)(\omega_n + \omega)} [(\omega \cos(\omega t + \phi) - i\omega_n \sin(\omega t + \phi)) - (\omega \cos(\phi) - i\omega_n \sin(\phi)) \exp(-i\omega_n t)]. \quad (40)$$

In the limit that $t \rightarrow \infty$, the term containing $\exp(-i\omega_n t) \rightarrow 0$ because ω_n contains a damping component as well as an oscillatory component, so the system forgets its initial conditions. In this limit, the solution is

$$328 \quad \mathbf{u}_\ell(r, t) = \sum_n \tilde{\mathbf{u}}_\ell(r; \omega_n) \frac{\langle \tilde{\mathbf{u}}_{\ell,h}^\dagger(\omega_n), \zeta(\mathbf{r}) \rangle}{(\omega_n - \omega)(\omega_n + \omega)} (\omega \cos(\omega t + \phi) - i\omega_n \sin(\omega t + \phi)). \quad (41)$$

The solution has a cosine component and a sine component, with respective amplitudes

$$330 \quad \mathcal{A}_{c,n} = \omega \frac{\langle \tilde{\mathbf{u}}_{\ell,h}^\dagger(\omega_n), \zeta(\mathbf{r}) \rangle}{(\omega_n - \omega)(\omega_n + \omega)}, \quad \mathcal{A}_{s,n} = -i\omega_n \frac{\langle \tilde{\mathbf{u}}_{\ell,h}^\dagger(\omega_n), \zeta(\mathbf{r}) \rangle}{(\omega_n - \omega)(\omega_n + \omega)} \quad (42)$$

Any field (e.g., velocity, entropy, or surface luminosity) can be expressed in terms of these amplitudes in the form

$$332 \quad \mathbf{u}_\ell(r, t) = \left(\sum_n \tilde{\mathbf{u}}_\ell(r; \omega_n) \mathcal{A}_{c,n} \right) \cos(\omega t + \phi) + \left(\sum_n \tilde{\mathbf{u}}_\ell(r; \omega_n) \mathcal{A}_{s,n} \right) \sin(\omega t + \phi). \quad (43)$$

The observed amplitude at a given forcing frequency ω is therefore the quadrature sum of the real component of the amplitude,

$$335 \quad |\mathbf{u}_\ell(r, \omega)| = \left[\left(\Re \left[\sum_n \tilde{\mathbf{u}}_\ell(r; \omega_n) \mathcal{A}_{c,n} \right] \right)^2 + \left(\Re \left[\sum_n \tilde{\mathbf{u}}_\ell(r; \omega_n) \mathcal{A}_{s,n} \right] \right)^2 \right]^{1/2}. \quad (44)$$

where $\Re()$ is the real operator.

Note that the derivation of Lecoanet et al. (2019) defined a forcing in their appendix A Eqn. 13 that differed from our Eqn. 37 in the following ways:

- 339 1. They produced a purely horizontal forcing by forming the forcing term from an angular gradient of a spherical
340 harmonic, which introduced additional factors of $\sqrt{\ell(\ell+1)}$ into their amplitude equation.
- 341 2. They used a complex forcing $\exp(i\omega t)$, whereas here we assume a purely real forcing $\sin(\omega t + \phi)$. While similar, the
342 imaginary components from an $\exp(i\omega t)$ forcing can interact with imaginary components of e.g., $\tilde{\mathbf{u}} \langle \tilde{\mathbf{u}}_\ell^\dagger(r; \omega_n), \zeta(\mathbf{r}) \rangle$
343 to produce unphysical contributions to the real amplitude. These amplitude contributions do not exist when
344 convection stochastically excites waves in stars or simulations, because that excitation is real, and our use of a
345 purely real forcing here corrects this error in previous work.

In order to proceed further, we need a model for the convective forcing, ζ .

347 3.4. Connecting the wave luminosity and the forcing

348 We will now derive a model for the forcing by convection. In our simulations, we will measure the convective wave
 349 luminosity as a proxy for the convective excitation. We will show in Section 3.4.1 how the wave luminosity relates to
 350 the wave radial velocity. Then, we will assume that the convective wave excitation can be approximated as a delta
 351 function forcing in radius, and we will derive the wave radial velocity response to many of these delta function forcings.
 352 Putting these together, we will create a link between the wave luminosity and a delta function forcing which can be
 353 used for ζ in Eqn. 42.

354 3.4.1. Connecting the wave luminosity to the wave velocity

355 The wave luminosity is convenient to measure because, in the limit of small dissipation, it does not vary with radius
 356 for radii larger than the forcing radius. We measure the wave luminosity,

$$357 L_w \equiv 4\pi r^2 \hat{H}^* \hat{u}_r, \quad (45)$$

358 where $H = (c_p \mu / \mathcal{R}) P$ is the enthalpy. The wave *flux* near the radiative-convective boundary is then

$$359 F_w = \hat{H}^* \hat{u}_r = \frac{L_w(f, \ell; A, \alpha, \beta)}{4\pi r_{rcb}^2}. \quad (46)$$

360 The wave motions follow the polarization relations (see section 8) such that the wave enthalpy can be expressed in
 361 terms of the wave velocity and a multiplicative factor,

$$362 h = \mathcal{P} u_r, \quad \text{with} \quad \mathcal{P}(N^2; \omega, k_h) = \rho_0 \frac{c_P \mu}{\mathcal{R}} \frac{\omega}{k_h^2} [-k_r(N^2, \omega, k_h) + i H_\rho^{-1}] \quad (47)$$

363 We will assume that $-k_r + i H_\rho^{-1} \approx -k_r$ such that the radial wavelength of the wave is small compared to changes of
 364 the stellar density stratification; this choice makes \mathcal{P} purely real. Note that per the dispersion relation (see section
 365 8), k_r is a function of N^2 and thus \mathcal{P} is a function of N^2 and ρ_0 , which both depend upon the radius. In evaluating
 366 Eqn. 47, we use the maximum N^2 in the inner 93% of the star, which we call N_{\max}^2 . We make this choice so that we
 367 can evaluate the transfer function at high frequency, because otherwise the dispersion relation $k_r \sim k_h \sqrt{N^2/\omega^2 - 1}$
 368 becomes imaginary at high frequency. However, this choice leads to an improper evaluation of the polarization relation
 369 $\mathcal{P} \propto k_r$ at low frequency. To correct this, we introduce a factor and define

$$370 \mathcal{P}'(r_{\text{force}}) = \frac{N(r_{\text{force}})}{N_{\max}} \mathcal{P}(N_{\max}). \quad (48)$$

371 We specify $r_{\text{force}} = 1.03$ where $r = 1$ is the core convection zone boundary.

372 We use this relation to express the wave radial velocity in terms of the wave luminosity,

$$373 |u_r|^2 = \frac{L_w(f, \ell; A, \alpha, \beta)}{4\pi r_{rcb}^2 \mathcal{P}'}. \quad (49)$$

374 3.4.2. Connection between mode velocity and bulk forcing

375 For simplicity, we assume that the excitation of waves can be approximated as a delta function forcing at a specific
 376 radial coordinate. Deriving the wave response to this delta function forcing in full spherical geometry and in the fully
 377 compressible equations is a difficult task. As a simplified model, we will derive the wave response of an incompressible,
 378 Boussinesq fluid in plane-parallel geometry (gravity in the \hat{z} direction) to a horizontal forcing of the desired form.
 379 Then we will assume that the derived expression linking wave vertical velocity and wave forcing is a universal response
 380 and can be used to link wave radial velocity to an angular forcing in spherical geometry. The following derivation
 381 closely follows appendix B of Lecoanet et al. (2019).

382 Eqns. 20-23 of Lecoanet et al. (2019) derive an expression for the average amplitude of the vertical velocity u_z of
 383 a plane-parallel wave in a domain spanning $z \in [0, L]$ and forced at one of the boundaries ($u_z(z=0) = F_B \sin(\omega t)$).
 384 They find a solution

$$385 u_z = F_B \left[\cos(k_z z) - \frac{\cos(k_z L)}{\sin(k_z L)} \right] \sin(\omega t) \quad (50)$$

386 with amplitude

$$387 \quad |u_z| = \left(\left| \frac{1}{L} \int_0^L u_z^2 dz \right| \right)^{1/2} = \sqrt{\frac{F_B^2}{2} \sin^{-2}(k_z L) \left\{ 1 + \frac{1}{k_z L} \cos(k_z L) \sin(k_z L) \right\}} \approx \sqrt{\frac{1}{2} \frac{F_B}{|\sin(k_z L)|}}, \quad (51)$$

388 where since the waves must satisfy $k_z L = n\pi$ for integer n , we have neglected terms of magnitude $1/\sqrt{k_z L}$ in the final
389 expression. This provides an expression for the resultant wave velocity due to a known, forced wave velocity at the
390 boundary. We will next derive an expression for the amplitude of waves that are forced in the bulk, then connect them
391 to this model for waves forced at a boundary.

392 We assume impenetrable boundary conditions in a plane-parallel layer ($u_z = 0$ at $z = 0$ and at $z = L$) and introduce
393 a bulk forcing,

$$394 \quad \partial_t \mathbf{u} + \nabla p - \rho \mathbf{g} = F_{\omega, k_h} \delta(z - z_f) \cos(\omega t) \mathcal{G}(\mathbf{x}). \quad (52)$$

395 We decompose the gradient operator $\nabla = \nabla_h + \partial_z \hat{z}$ and assume that the forcing is purely horizontal, $\nabla \cdot \mathcal{G} = \nabla_h \cdot \mathcal{G} =$
396 $ik_h \mathcal{G}$. Going forward, we assume $\mathcal{G}(\mathbf{x}_h) = e^{-ik_h x}$, so that all of its amplitude is encoded in F_{ω, k_h} . Our Eqn. 52 differs
397 from Eqn. 24 of Lecoanet et al. (2019) in that we do not assume that \mathcal{G} is formed from a horizontal gradient, so
398 our solution differs by a factor of k_h . We dot ∇_h into the above equation and apply the continuity equation in the
399 incompressible regime ($\nabla \cdot \mathbf{u} = \nabla_h \mathbf{u}_h + \partial_z u_z = 0$) to obtain

$$400 \quad -\partial_t \partial_z u_z + \nabla_h^2 p = ik_h F_{\omega, k_h} \delta(z - z_f) \cos(\omega t) \mathcal{G}(\mathbf{x}_h), \quad (53)$$

401 We now integrate vertically from $z^- = z_f - \epsilon$ to $z^+ = z_f + \epsilon$ in the limit that $\epsilon \rightarrow 0$, define $\Delta u_z = \int_{z^-}^{z^+} \partial_z u_z dz$, and
402 apply the condition that $\partial_z u_z$ is continuous at z_f , to find

$$403 \quad \partial_t \Delta u_z = -ik_h F_{\omega, k_h} \cos(\omega t) \mathcal{G}(\mathbf{x}_h). \quad (54)$$

404 Integrating that in time under the boundary condition that $\Delta u_z(t = 0) = 0$, we get an expression for our final boundary
405 condition: the jump in Δu_z across the forcing,

$$406 \quad \Delta u_z = -i \frac{k_h}{\omega} F_{\omega, k_h} \sin(\omega t) \mathcal{G}(\mathbf{x}_h). \quad (55)$$

407 Writing the solution as

$$408 \quad u_z = \begin{cases} A \cos(k_z z) + B \sin(k_z z) & z < z_f, \\ C \cos(k_z z) + D \sin(k_z z) & z > z_f \end{cases}, \quad (56)$$

409 we set

$$410 \quad u_z(z = 0) = 0, \quad u_z(z = L) = 0, \quad \partial_z u_z(z = z^-) = \partial_z u_z(z = z^+), \quad u_z(z = z^-) + \Delta u_z = u_z(z = z^+), \quad (57)$$

411 and retrieve the solution

$$412 \quad u_z = -\Delta u_z \begin{cases} \left[\cos(k_z z_f) \frac{\cos(k_z L)}{\sin(k_z L)} + \sin(k_z z_f) \right] \sin(k_z z) & z < z_f \\ \frac{\cos(k_z z_f)}{\sin(k_z L)} \sin(k_z(z - L)) & z > z_f \end{cases}. \quad (58)$$

413 Averaging over the region above z_f provides an expression for the average forced velocity,

$$414 \quad \overline{u_z^2} = \frac{1}{L - z_f} \int_{z_f}^L u_z^2 dz = -\frac{(\Delta u_z)^2}{2} \frac{\cos^2(k_z z_f)}{\sin^2(k_z L)} + \mathcal{O}\left(\frac{1}{k_z L}\right). \quad (59)$$

415 If the system is forced at a node of an eigenfunction, that mode will be “missing” from the response. In order to
416 ensure that all modes are excited, we assume that the system responds to many delta-function forcings of magnitude
417 F_{ω, k_h} over a vertical range Δz , producing an average response of

$$418 \quad |u_z|_\Delta^2 = \frac{1}{\Delta z} \int_{z_0}^{z_0 + \Delta z} \overline{u_z^2}(z_f) dz_f = -\frac{(\Delta u_z)^2}{4 \sin^2(k_z L)} + \mathcal{O}\left(\frac{1}{k_z \Delta z}\right), \quad (60)$$

where we have assumed that $k_z \Delta z \gg \pi$ such that

$$\frac{1}{\Delta z} \int_{z_0}^{z_0 + \Delta z} \cos^2(k_z z_f) dz = \frac{1}{m\pi} \int_0^{m\pi} \cos^2(\theta) d\theta \approx \frac{1}{2} \quad (61)$$

for $m \gg 1$. Neglecting terms of order $\sqrt{1/(k_z \Delta z)}$, the wave response amplitude to many delta function bulk forcing terms is

$$|u_z|_\Delta = \sqrt{\bar{u}_z^2} \approx \frac{k_h}{2\omega} \frac{F_{\omega, k_h}}{|\sin(k_z L)|}. \quad (62)$$

This amplitude is identical to the case of the boundary forcing response in Eqn. 51 under the relation

$$F_{\omega, k_h} = \sqrt{2} \frac{\omega}{k_h} F_B. \quad (63)$$

Now we recall that the boundary forcing was achieved by specifying $u_z = F_B$ at the boundary. We therefore assume that by Eqn. 63, we can relate the bulk forcing to the vertical velocity magnitude.

$$F_{\omega, k_h} = \sqrt{2} \frac{\omega}{k_h} u_z. \quad (64)$$

As in Lecoanet et al. (2019), we hypothesize that this relationship is universal and holds true in spherical coordinates, replacing u_z with u_r . However, note that our Eqn. 64 differs from Lecoanet et al. (2019), Appendix B, Eqn. 29 by a factor of k_h^{-1} , which arises from our differing definition of \mathcal{G} , and a constant factor $(\sqrt{2})/(\pi/2)$, which arises from our choice of a different averaging operation in Eqn. 60.

3.4.3. Forcing specification used in amplitude equation

As a simplified model, we will assume that waves are excited via a horizontal bulk delta-function forcing near the radiative-convective boundary,

$$|\zeta(r)| = F_{\omega, k_h} \delta(r - r_{\text{rcb}}). \quad (65)$$

The amplitude of this bulk forcing can be specified in terms of the wave luminosity by combining Eqns. 49 and 64,

$$F_{\omega, k_h} = \frac{\omega}{k_h} \left(\frac{L_w(f, \ell; A, \alpha, \beta)}{2\pi r_{\text{rcb}}^2 \mathcal{P}'} \right)^{1/2}. \quad (66)$$

3.5. Formulae for surface perturbations given the wave luminosity

The surface manifestation of the magnitude perturbations caused by the gravity waves can now be retrieved. The cosine and sine amplitudes of the solution are

$$\mathcal{A}'_{c,n}(\omega, \ell) = \frac{\mathcal{A}_{c,n}(\omega, \ell)}{\sqrt{L_w(\omega, \ell)}} = \frac{\omega}{(\omega_n - \omega)(\omega_n + \omega)} \left(2\rho_0 \frac{\omega}{k_h} (\mathbf{u}_\ell^\dagger)^* \sqrt{2\pi r^2 \frac{1}{\mathcal{P}'}} \right) \Big|_{r=r_{\text{rcb}}}, \quad (67)$$

$$\mathcal{A}'_{s,n}(\omega, \ell) = \frac{\mathcal{A}_{s,n}(\omega, \ell)}{\sqrt{L_w(\omega, \ell)}} = \frac{-i\omega_n}{(\omega_n - \omega)(\omega_n + \omega)} \left(2\rho_0 \frac{\omega}{k_h} (\mathbf{u}_\ell^\dagger)^* \sqrt{2\pi r^2 \frac{1}{\mathcal{P}'}} \right) \Big|_{r=r_{\text{rcb}}}. \quad (68)$$

The transfer function for the photometric variability at the surface due to a single delta function forcing is therefore

$$T_r(\omega, \ell, r_{\text{rcb}}) = \left[\left(\Re \left[\sum_n \widetilde{\Delta m_\ell}(R_*; \omega_n) \mathcal{A}'_{c,n} \right] \right)^2 + \left(\Re \left[\sum_n \widetilde{\Delta m_\ell}(R_*; \omega_n) \mathcal{A}'_{s,n} \right] \right)^2 \right]^{1/2}. \quad (69)$$

The link between the mode amplitude and the wave luminosity (the transfer function) is only valid if the response is evaluated for many delta function forcings spread over a range of radii. We perform an analogous operation to Eqn. 60 and evaluate the mean power of the transfer response of $N_F = 200$ radially evenly spaced delta function forcings (r_{rcb}) between $r = 0.97$ and $r = 1.03$ (where $r = 1$ is the convective core boundary),

$$T(\omega, \ell) = \left[\frac{1}{N_F} \sum_{i=1}^{N_F} T_r^2(\omega, \ell, r_i) \right]^{1/2}. \quad (70)$$

452 The photometric variability at a given ℓ and ω can then be constructed from the wave luminosity and transfer function,

453
$$|\Delta m|(\omega, \ell) = T(\omega, \ell) \sqrt{L_w(\omega, \ell)}. \quad (71)$$

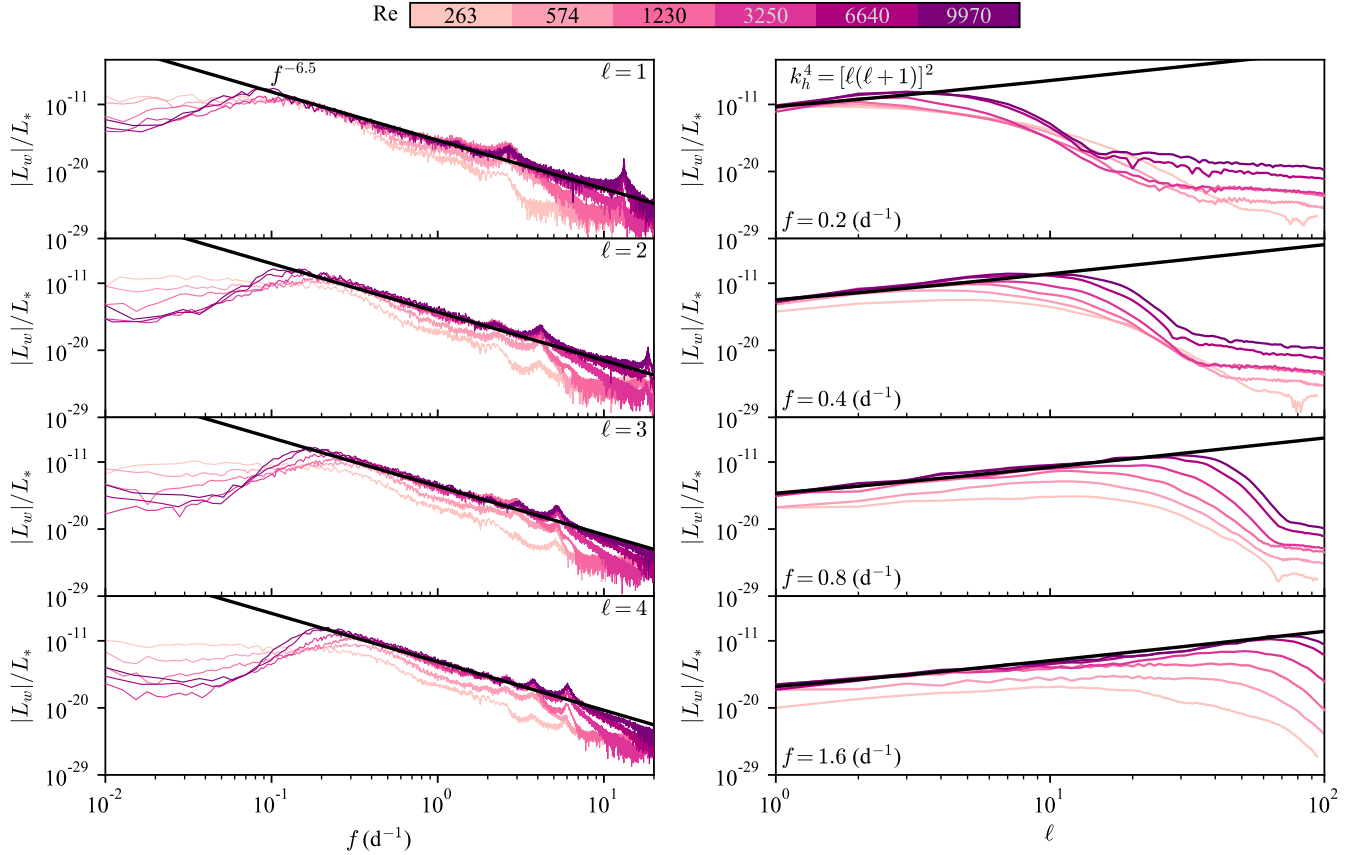


Figure 2. We plot the absolute value of the wave luminosity normalized by the stellar luminosity in Wave Generation simulations of our $15 M_\odot$ model. (Left panels) Shown is the wave luminosity spectrum vs. frequency at $\ell = [1, 2, 3, 4]$ (from top to bottom). (Right panels) Shown is the wave luminosity spectrum vs. ℓ at $f = [0.2, 0.4, 0.8, 1.6] \text{ d}^{-1}$ (from top to bottom). Lines are colored by the Reynolds number of the simulation (see Table 3), with the most turbulent simulation being the darkest line. The black line shows the fit from Eqn. 74 for the $15 M_\odot$ star.

4. THE WAVE LUMINOSITY SPECTRUM IN WAVE GENERATION SIMULATIONS

4.1. Wave flux saturation at high Reynolds number

We perform many Wave Generation simulations of the $15 M_\odot$ model where we simultaneously increase the spatial resolution while decreasing the diffusivity, see Table 3. We measure the wave luminosity spectrum at a nondimensional $r = 1.25$. We plot the wave luminosity at $\ell = [1, 2, 3, 4]$ and $f = [0.2, 0.4, 0.8, 1.6] \text{ d}^{-1}$ in Fig. 2. We find a wave luminosity spectrum that can be fit to a power-law $L_w \propto f^{-13/2} k_h^4$, with $k_h = \sqrt{\ell(\ell+1)}$. Although we only plot a few values of ℓ and f , we verified that these power-laws work well for many other values, and the full wave luminosity data cubes are available online in a Zenodo repository (Anders et al. 2023). This wave luminosity spectrum was theoretically predicted by Lecoanet & Quataert (2013) and observed in simulations run using the Dedalus (Couston et al. 2018; Lecoanet et al. 2021) and MAGIC codes (Le Saux et al. 2022), but is very different from the plume-based wave energy spectrum observed by Rogers et al. (2013). As the diffusion lowers and turbulence increases, we find that the wave luminosity increases at frequencies $f \gtrsim 0.3 \text{ d}^{-1}$. Once the diffusivities are decreased enough to reach $\text{Re} \gtrsim 2000$ (requiring 512 degrees of freedom across the CZ), the wave luminosity ceases to increase as the diffusivities are further decreased. We therefore conclude that the wave luminosity is numerically converged once there are 512 degrees of freedom across the CZ, and we run our Wave Generation simulations for the 3 and $40 M_\odot$ models with this grid resolution.

We do note that further decreasing the diffusivity changes the range of the frequencies (at low frequency) and spherical harmonic degrees (high ℓ) that are filled by the powerlaw wave luminosity spectrum. In a star, we would therefore expect this power law to extend down to very low frequency (to the frequency at which convection drives

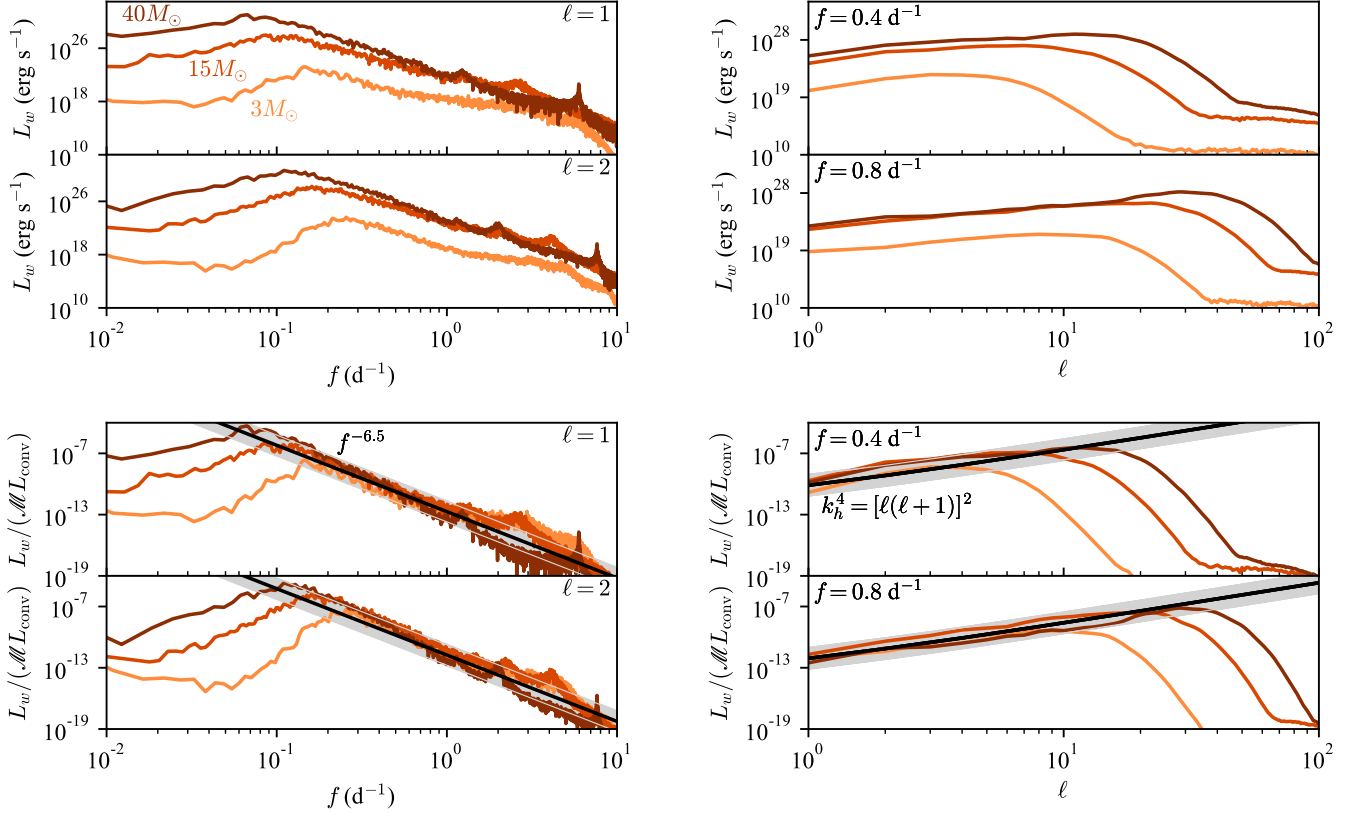


Figure 3. We plot the wave luminosity spectra from Wave Generation simulations with 512 resolution elements across the convection zone for the $3 M_{\odot}$ (light orange), $15 M_{\odot}$ (dark orange), and $40 M_{\odot}$ (brown) models. As in Fig. 2, we plot the spectra vs. frequency in the left panel at $\ell = [1, 2]$ and vs. ℓ in the right panel at $f = [0.4, 0.8] \text{ d}^{-1}$. In the top four panels, we plot the wave luminosity in cgs units. In the bottom four panels, we divide by $\mathcal{M}L_{\text{conv}}$, where \mathcal{M} is the characteristic convective Mach number of core convection and L_{conv} is the core convective luminosity. The black line and greyed band show the range of fits quoted in Eqn. 72.

473 the waves), and up to very high spherical harmonic degree. Note also that the wave luminosity spectrum includes
 474 small resonant peaks, such as the one around 1.5 d^{-1} . These peaks occur because our wave damping layer does not
 475 fully damp out these high frequency waves. We have tried increasing and decreasing the radial extent and forcing
 476 magnitude of the wave damping layer, and found the settings that we used to work well for damping most waves.

477 4.2. Wave fluxes of different stars

478 Having verified the resolution required to achieve a reliable measure of the wave luminosity, we now run Wave
 479 Generation simulations of stellar models of different masses. We plot the measured wave luminosities in the top panels
 480 of Fig. 3 for $\ell = [1, 2]$ and $f = [0.4, 0.8] \text{ d}^{-1}$. We find similar spectra for all three stars in this work. The $3 M_{\odot}$
 481 and $15 M_{\odot}$ are well-described by a $L_w \propto f^{-13/2} k_h^4$; the wave luminosity spectrum of the $40 M_{\odot}$ star seems to vary
 482 more steeply with frequency, perhaps $L_w \propto f^{-15/2} k_h^4$, which has also been seen in simulations performed by Lecocanet
 483 et al. (2021) and Le Saux et al. (2022). Regardless, since a spectrum of the form $L_w \propto f^{-13/2} k_h^4$ is theoretically
 484 expected, and since this spectrum describes the $3 M_{\odot}$ and $15 M_{\odot}$ stars well, and also describes the $40 M_{\odot}$ star fairly
 485 well below $f \lesssim 0.3 \text{ d}^{-1}$ where the wave luminosity signal is strongest, we will describe the wave luminosity spectrum
 486 using $L_w \propto f^{-13/2} k_h^4$.

487 In the bottom panels of Fig. 3, we plot the same wave luminosities, but normalized by $\mathcal{M}L_{\text{conv}}$, where $\mathcal{M} =$
 488 $\{1.30, 5.33, 9.48\} \times 10^{-4}$ are the volume-averaged convective mach numbers in the core convection zones for the
 489 $\{3, 15, 40\} M_{\odot}$ stars and $L_{\text{conv}} = \{5.85 \times 10^{34}, 1.90 \times 10^{37}, 2.28 \times 10^{38}\} \text{ erg s}^{-1}$ are the convective luminosities of

490 the core convection. The wave luminosities seem to follow a universal powerlaw of the form

$$491 \quad L_w = (4 \times 10^{-46 \pm 1}) \mathcal{M} L_{\text{conv}} \left(\frac{f}{\text{Hz}} \right)^{-13/2} (\ell[\ell+1])^2, \quad (72)$$

492 and we plot this line and also the uncertainty range of our exponent as a black line and grayed stripe in Fig. 3. We
 493 note that we theoretically expect a general powerlaw of the form (Lecoanet & Quataert 2013; Goldreich & Kumar
 494 1990)

$$495 \quad L_w \approx \mathcal{M} L_{\text{conv}} \left(\frac{f}{f_c} \right)^{-13/2} (\ell[\ell+1])^2, \quad (73)$$

496 where f_c is the characteristic frequency of the core convection. The three stars studied in this work have $f_c =$
 497 $u_{\text{MLT}}/R_{\text{core}} = \{4.78, 5.30, 3.93\} \times 10^{-7}$ Hz for the $\{3, 15, 40\} M_\odot$ stars, so we do not sample enough dynamic range of
 498 f_c to characterize that scaling. We fit in log-space the $f^{-13/2} (\ell[\ell+1])^2$ spectrum to L_w for each of the stars at $\ell = 1$
 499 and in the range $f = [0.2, 1.5] \text{ d}^{-1}$ ($3 M_\odot$), $f = [0.2, 1] \text{ d}^{-1}$ ($15 M_\odot$), and $f = [0.1, 0.7] \text{ d}^{-1}$ ($40 M_\odot$). These fits are,

$$500 \quad L_w = \left\{ \begin{array}{ll} 7.34 \times 10^{-15} \text{ erg s}^{-1} & (\text{for } 3M_\odot) \\ 2.33 \times 10^{-11} \text{ erg s}^{-1} & (\text{for } 15M_\odot) \\ 5.30 \times 10^{-10} \text{ erg s}^{-1} & (\text{for } 40M_\odot) \end{array} \right\} \left(\frac{f}{\text{Hz}} \right)^{-13/2} (\ell[\ell+1])^2, \quad (74)$$

501 and we will use these when we generate our photometric variability predictions in Section 6.

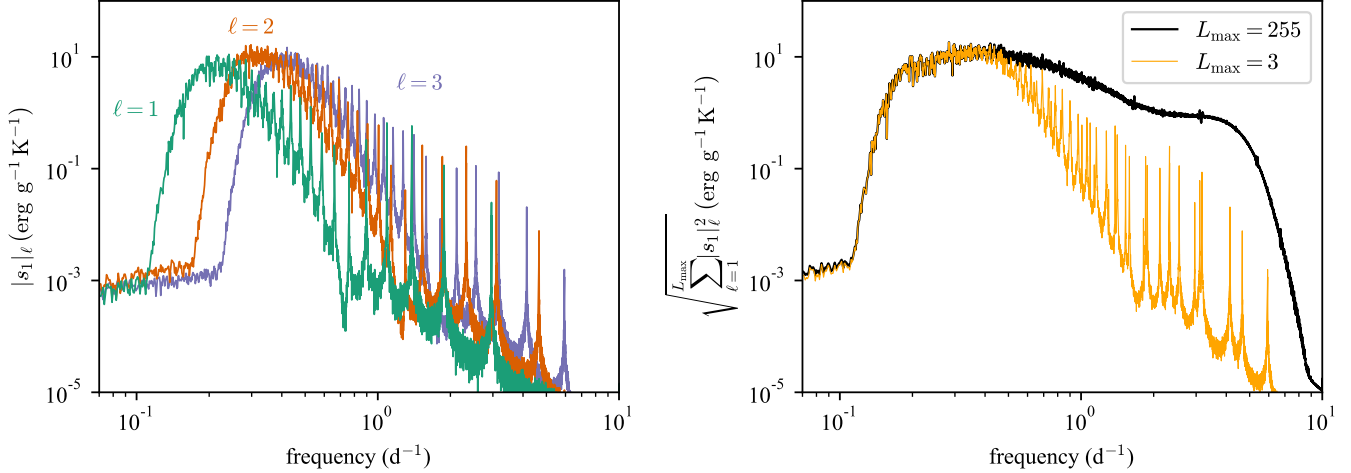


Figure 4. We plot the amplitude spectrum of entropy perturbations at the outer boundary of the wave propagation simulation. (Left panel) individual contributions to the surface amplitude spectrum from the first three spherical harmonics. (Right panel) Summed entropy amplitude fluctuations over (orange) the first three spherical harmonics and (black) all spherical harmonics. Note that these sums account for all power over the full 4π of the simulation surface; “realistic” observations observing only one hemisphere must account for cancellation effects, see Sec. 6.

5. VERIFICATION OF THE TRANSFER FUNCTION IN WAVE PROPAGATION SIMULATIONS

5.1. Surface perturbations of standing gravity waves

We now examine the Wave Propagation simulation to verify our method for determining the surface variability using the transfer function.

We sample the entropy perturbations at the surface of the wave propagation simulation every 30 minutes over the course of the last ~ 1.7 years of simulated time⁶. We plot the amplitude spectrum of those entropy perturbations in Fig. 4. In the left panel of Fig. 4, we plot the frequency spectrum of the entropy perturbations of the first three spherical harmonics. We see that the shape of the signal at each ℓ is characterized by three features: (1) high-amplitude resonant peaks at high frequency, (2) the imprinted spectrum of convective driving which decreases in amplitude as the frequency increases, and (3) strong radiative damping of gravity waves at low frequencies. In the right panel of Fig. 4, we show the quadrature sum of the three signals in the left panel (yellow line) as well as the quadrature sum over all ℓ values in this simulation (black line). When summing over all ℓ values, we observe a relatively flat noise-like signal. We note that the power at high ℓ would not be visible in photometric observations due to cancellation over a single hemisphere (see Sec. 6.1), but we still include them in our calculations. In total, this simulation was run for ~ 5 years to allow the power in the standing modes to develop.

5.2. Calculation of the transfer function for the Wave Propagation simulation

We now calculate a transfer function which describes how the environment of the Wave Propagation simulation modifies the convective luminosity. To do so, we calculate the eigenvalues and eigenfunctions associated with the gravity waves in the simulation’s wave cavity using **Dedalus** following the prescription described in section 2.

5.2.1. Timestepping errors in high-frequency waves

Before directly computing the transfer function, we first note that timestepping errors in simulations can alter the eigenvalues of gravity waves which propagate in the simulation domain. We must account for these errors before computing the transfer function associated with our simulation.

We evolve the simulations in this paper using **Dedalus**’ SBDF2 timestepper, which is the second order semi-implicit backward difference scheme presented in Wang & Ruuth (2008). Timestepping truncation errors can modify a wave’s oscillation frequency and damping rate, and this can affect the measured signal of waves in our simulations. Consider

⁶ Recall from Table 2 that the characteristic dynamical timescale of convection is $t_{\text{heat}} = 4.66 \times 10^5$ s ≈ 5.4 days.

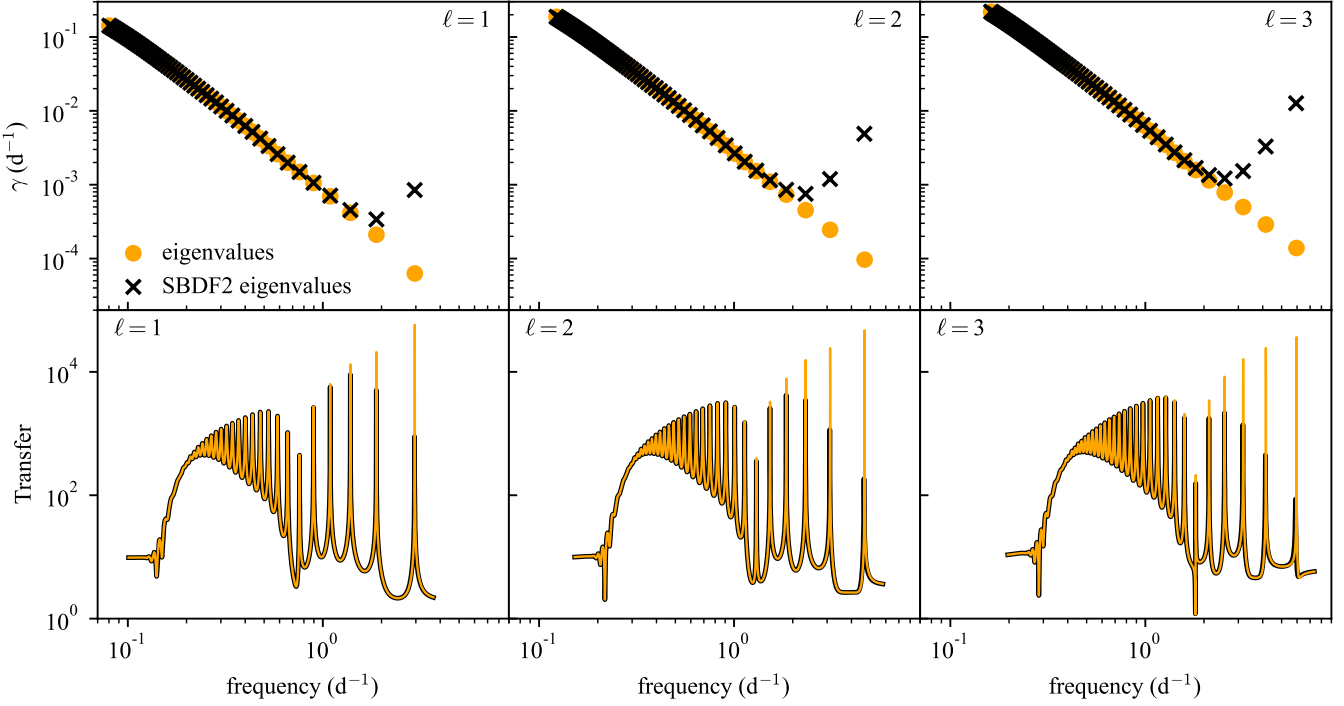


Figure 5. (Top panels) The spectra of the imaginary vs. real components of the gravity wave eigenvalues for the Wave Propagation simulation for $\ell = 1$ (left), $\ell = 2$ (middle), and $\ell = 3$ (right); orange values are directly obtained from the eigenvalue solve while black values indicate how the orange values change after applying Eqn. 80, i.e., with the effects of SBDF2 timestepping included, assuming $\Delta t = 2.98 \times 10^{-3} d$, which was a typical timestep size for the Wave Propagation simulation. (Bottom panels) The transfer function calculated using the real eigenvalues (orange) and the SBDF2 eigenvalues (black). Note that the highest frequency waves which should be damped the least achieve much smaller peaks with lower quality factors due to timestepping errors.

528 a simple damped wave,

$$\partial_t u = -i\tilde{\omega}u, \quad (75)$$

530 where $\tilde{\omega} = \omega - i\gamma$ with $\gamma > 0$ the damping rate and ω the oscillation angular frequency. Time steps of size Δt follow
531 the form

$$\frac{1}{\Delta t} \left(\frac{3}{2}U^n - 2U^{n-1} + \frac{1}{2}U^{n-2} \right) = -i\tilde{\omega}U^n, \quad (76)$$

533 where the solution at the next time step U^n is solved from U^{n-1} and U^{n-2} —the respective values of the numerical
534 solution at the two preceding time steps.

535 To approximate the trajectory of the numerical solution, we seek an effective $\tilde{\omega}_{\text{eff}}$ such that

$$U^n = (e^{-i\tilde{\omega}_{\text{eff}}\Delta t})^n U^0 = e^{-i\tilde{\omega}_{\text{eff}}n\Delta t} U^0. \quad (77)$$

537 Substituting this form into Eqn. 76, we obtain a quadratic polynomial in $A = e^{-i\tilde{\omega}_{\text{eff}}\Delta t}$ given by

$$(3 + i2\tilde{\omega}\Delta t) A^2 - 4A + 1 = 0, \quad (78)$$

539 with roots

$$A_{\pm} = \frac{2 \pm \sqrt{1 - i2\tilde{\omega}\Delta t}}{3 + i2\tilde{\omega}\Delta t}. \quad (79)$$

541 Here A_+ is the principal root corresponding to the actual numerical trajectory, and A_- is a spurious root that does
542 not correspond to the numerical solution. Hence, the exact relation describing the SBDF2 modification of the gravity
543 wave eigenvalues is given by

$$-i\tilde{\omega}_{\text{eff}}\Delta t = \log(A_+). \quad (80)$$

Accordingly, the timestepped wave has an effective (i.e., numerical) oscillation frequency $\omega_{\text{eff}} = \text{Re}(\tilde{\omega}_{\text{eff}})$ and damping rate $\gamma_{\text{eff}} = -\text{Im}(\tilde{\omega}_{\text{eff}})$.

An asymptotic analysis of Eqn. 80 can be performed to establish the significance of these effective parameters. Expanding $\log(A_+)$ in the limit of $|i\tilde{\omega}\Delta t| < 1$ we obtain

$$-i\tilde{\omega}_{\text{eff}}\Delta t = \log(A_+) = -\left((i\tilde{\omega}\Delta t) + \frac{1}{3}(i\tilde{\omega}\Delta t)^3 + \frac{1}{4}(i\tilde{\omega}\Delta t)^4 + \mathcal{O}(\Delta t^5)\right). \quad (81)$$

Rearranging, we find

$$\tilde{\omega}_{\text{eff}} = \tilde{\omega} - \frac{1}{3}\tilde{\omega}^3\Delta t^2 - i\frac{1}{4}\tilde{\omega}^4\Delta t^3 + \mathcal{O}(\Delta t^4). \quad (82)$$

By inspecting the magnitude of the real and imaginary parts of Eqn. 82 we can infer information about the effective oscillation frequency and damping rate. When the wave damping timescale is much longer than that of the oscillations, i.e., $0 < \gamma \ll \omega$, we find at leading order that

$$\omega_{\text{eff}} = \omega - \frac{1}{3}\omega^3\Delta t^2 + \mathcal{O}(\Delta t^4), \quad (83)$$

and

$$\gamma_{\text{eff}} = \gamma + \frac{1}{4}\omega^4\Delta t^3 + \mathcal{O}(\Delta t^5). \quad (84)$$

Thus, in simulations of waves with long damping timescales, Eqn. 84 shows that the effective damping rate γ_{eff} is set by ω , which can lead to a drastically enhanced damping rate, sometimes several orders of magnitude larger than the original γ . By contrast, the effective oscillation frequency in Eqn. 83 experiences relatively little change.

In Fig. 5, we plot the gravity wave eigenvalues and transfer function associated with the wave cavity in our Wave Propagation simulation for the first three spherical harmonics $\ell = [1, 3]$. In the top panels, we plot the eigenvalues obtained from our eigenvalue solve, and the eigenvalues altered according to Eqn. 80 with $\Delta t = 2.98 \times 10^{-3}$ d, which is a typical timestep size for this simulation. We see that the timestepped solution matches the true eigenvalues for most modes and matches particularly well at low frequency. However, the damping rate of the highest frequency modes is greatly increased. In the case of the $\ell = 1$ modes, we might naively think that the lifetime of the longest-lived wave is $t_{\text{mode}} \sim 1/(6 \times 10^{-5})$ d = 46 years, but in our timestepped simulation the longest-lived wave actually has a lifetime of $t_{\text{mode}} \sim 1/(3 \times 10^{-4})$ d = 9 years. For comparison, the duration of our Wave Propagation simulations is ~ 5 years, which allows us to capture a significant portion of the longest mode lifetimes.

The bottom panels of Fig. 5 display the transfer functions⁷ calculated according to Eqn. 70 using the eigenvalues of the wave cavity (orange lines) and the eigenvalues of the wave cavity accounting for timestepping (black lines). We see that the associated changes in the mode lifetimes shown in the top panels also correspond to resonant peaks of much lower quality factor in the transfer function; for example, the quality factor of the peak of the highest frequency wave at $\ell = 3$ decreases by about three orders of magnitude, which is equal in magnitude to the change in the mode lifetime. Note also that at $\ell > 1$, the oscillatory portion of the highest frequency waves are also modestly affected by timestepping errors, which can be seen from the slight horizontal offset between the peaks of the yellow and black lines. Finally, we note that while the transfer function calculation here reproduces all of the expected wave features (resonant peaks and damping at low frequency), at very low frequencies the quality of the transfer function solution degrades. Since our mode expansion is finite rather than infinite, the calculation of the dual basis incurs errors which accumulate in the highest radial order (lower frequency) gravity modes, and these errors appear as a “noisy tail” to the left side of the transfer function; this feature of the signal is not physical.

5.2.2. Comparing Wave Propagation data with transfer function solution

In Fig. 6, we plot the measured surface entropy fluctuations from the Wave Propagation simulation (black lines) as well as the predicted surface entropy perturbations from Eqn. 71. To create this prediction, we multiply the transfer function (black lines in bottom panels of Fig. 5) and the square root of the measured wave luminosity from the Wave Generation simulation (the $15 M_\odot$ orange line in Fig. 3). We find excellent agreement between the Wave Propagation simulation data and the wave luminosity filtered through the transfer function solution, particularly at moderately

⁷ These transfer functions are for the *entropy* perturbation at the surface of our simulation rather than the *photometric variability* at the surface of the star, so we replace $\widetilde{\Delta m}_\ell(R_*; \omega_n)$ in Eqn. 69 with $\widetilde{s_{1,\ell}}(R_{\text{sim}}, \omega_n)$.

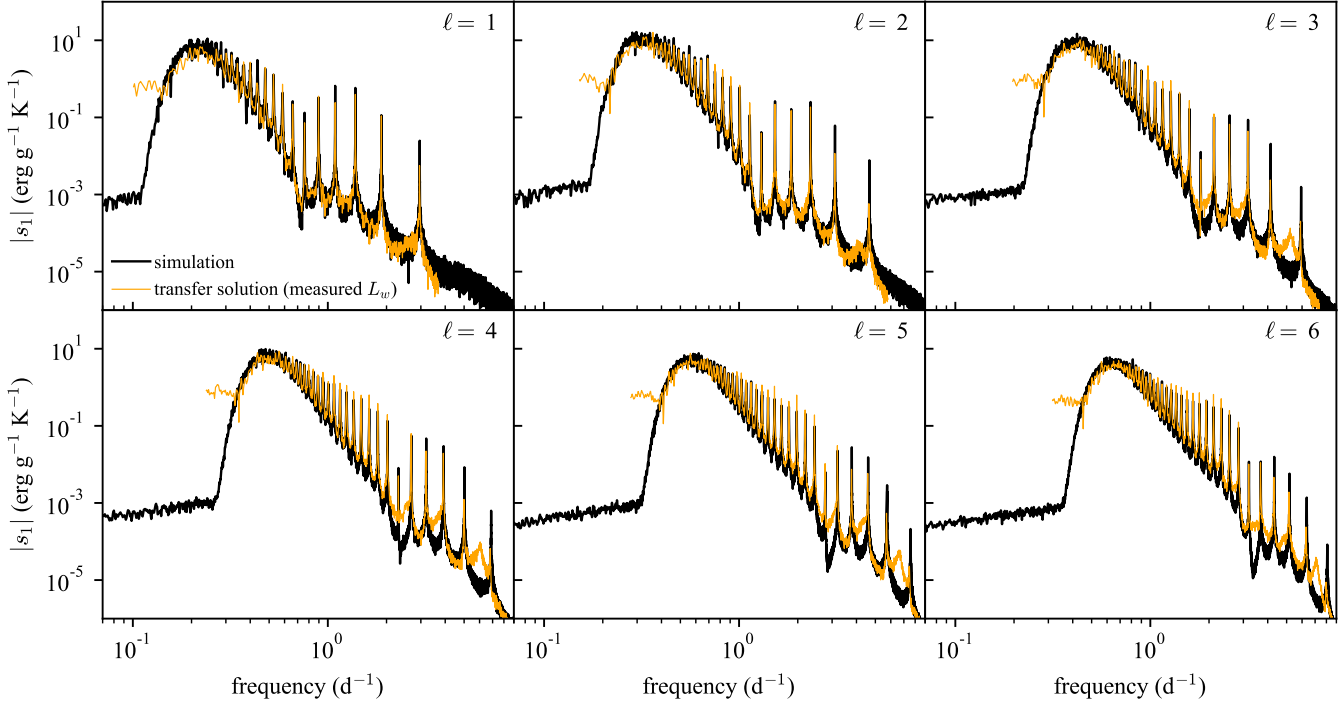


Figure 6. Shown are entropy amplitude perturbations at the surface of the Wave Propagation simulation (black lines) for the first six spherical harmonic degrees. Overplotted in orange are our predictions for the surface perturbations. We create the orange line by multiplying the transfer function (shown in bottom panels of Fig. 5) by the square root of the wave luminosity from the $15M_{\odot}$ Wave Generation simulation shown in Fig. 3. Note that the transfer functions have unphysical “tails” on their low-frequency edge; these tails are discussed in the final paragraph of Section 5.2.1.

588 low frequencies where the amplitude of the wave response is maximized. The transfer function captures the damping
 589 cutoff at low frequency, the decay of the spectrum baseline with increasing frequency, and the overall character of
 590 the standing mode peaks. We note that at higher values of ℓ , the mode peaks and continuum (troughs) are slightly
 591 over-predicted, and the amplitudes of the highest frequency modes at each ℓ are under-predicted, perhaps suggesting
 592 that our timestepping correction to the eigenmodes overestimates numerical damping in the simulation. However,
 593 if we had instead neglected to make the timestepping corrections introduced in Section 5.2.1, the amplitude of the
 594 highest-frequency peaks would have been vastly overestimated (e.g., the highest-frequency peaks in orange at $\ell = 1$
 595 and 2 would have amplitudes at least an order of magnitude higher than the peaks in black). Furthermore, standing
 596 mode peaks in the wave luminosity spectrum that are not perfectly damped by our damping layers (see Section 2.6
 597 and Fig. 3) result in unphysical bumps in the predicted solution at high ℓ (see e.g., at $f \gtrsim 0.2 \text{ d}^{-1}$ for $\ell = 4$).

598 In general, we want to describe the wave luminosity using a simple functional form. In Fig. 7, we plot the same
 599 quantities as in Fig. 6, but this time we convolve the transfer function with the powerlaw fit to the wave flux from
 600 Eqn. 74. Again, we find good agreement between the transfer function and the surface power of our simulations,
 601 particularly at $\ell = 1$. We find that as ℓ increases and at higher frequencies, the powerlaw wave luminosity overestimates
 602 the wave driving observed in our simulations; it is possible that particularly at higher ℓ , the true wave luminosity
 603 spectrum is steeper than the $f^{-13/2}$ spectrum we employ. However, the peak of the measured spectrum at low
 604 frequency which is the highest amplitude and most observable feature of the spectrum is still faithfully obtained,
 605 particularly at $\ell = 1$ which is the most available spherical harmonic degree to observations.

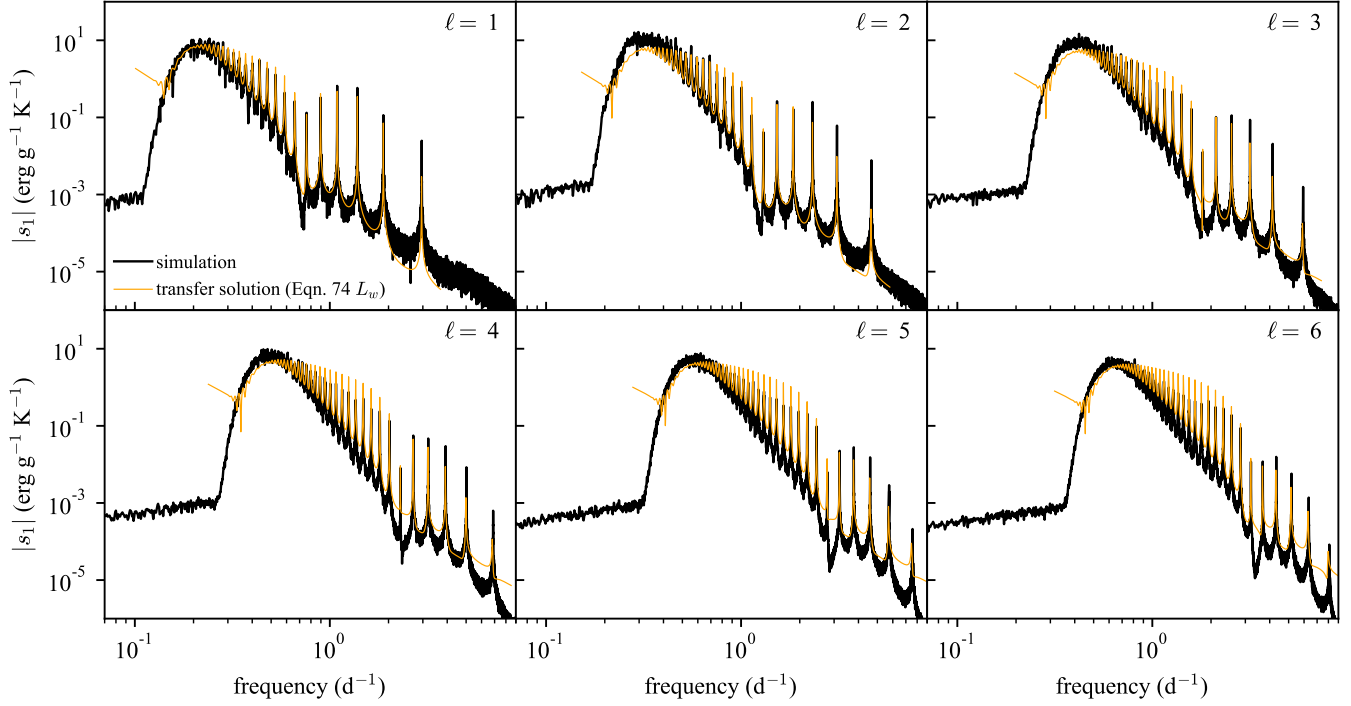


Figure 7. As in Fig. 6, but now we create the transfer function prediction by multiplying the transfer function by the best-fit to the wave luminosity shown in Eqn. 74.

6. PHOTOMETRIC VARIABILITY SPECTRA

Having measured the wave luminosity and verified our transfer function method, we now make predictions for what the observed photometric variability would be at the surface of a star. To do so, we must first calculate what the surface photometric magnitude fluctuations, properly convolved with an instrumental passband, would be for each eigenmode. With those values in hand for each mode, we can construct a transfer function and use that function to filter the wave luminosity from Eqn. 74.

6.1. GYRE g-modes and MSG surface magnitudes

We use GYRE (Townsend & Teitler 2013; Townsend et al. 2018, version 7.0) to calculate the nonadiabatic eigenvalues and eigenvectors associated with g-modes in our stellar models. GYRE finds a spectrum of dimensionless eigenmodes $\omega_n = \omega_{0,n} - i\gamma_n$ with real oscillation angular frequency $\omega_{0,n}$ and a real damping rate γ_n . Each mode has an associated eigenfunction for radial displacement $\tilde{\xi}_r$, horizontal displacement $\tilde{\xi}_\perp$ and luminosity δL . We follow the scaling convention of Eqns. 7-8 of Townsend et al. (2018) (which themselves align with the energy normalization in Eqn. 3.139 of Aerts et al. 2010) and construct dimensional eigenfunctions of arbitrary amplitude for the luminosity, displacement, and velocity as follows:

$$\delta L_n(r) = \sqrt{4\pi} L_* \tilde{\delta L}_n(r), \quad (85)$$

$$\xi_{n,r}(r) = \sqrt{4\pi} R_* \tilde{\xi}_{n,r}(r), \quad (86)$$

$$\xi_{n,\perp}(r) = \sqrt{4\pi} R_* \tilde{\xi}_{n,\perp}(r), \quad (87)$$

$$u_{n,r}(r) = -i \omega_{\text{cgs}} \xi_{n,r}(r), \quad (88)$$

$$u_{n,\perp}(r) = -i \omega_{\text{cgs}} \xi_{n,\perp}(r) \quad (89)$$

where $\omega_{\text{cgs}} = \sqrt{GM_*/R_*^3}\omega_n$ (Townsend & Teitler 2013, Eqn. A4).

6.1.1. Recovering surface magnitude perturbations for each mode with MSG

To calculate the magnitude fluctuation associated with a given gyre eigenmode, we follow the procedure laid out in Section 2 of Townsend (2003), which follows from earlier work, e.g., Dziembowski (1977). From the GYRE eigenmodes we calculate the perturbation coefficients associated with each wave,

$$\Delta_{R,n} = \sqrt{4\pi} \tilde{\xi}_{n,r}(R_*), \quad (90)$$

$$\Delta_{L,n} = \sqrt{4\pi} \tilde{\delta L}_n(R_*), \quad (91)$$

$$\Delta_{g,n} = -(2 + \omega_{0,n}^2) \Delta_{R,n}, \quad (92)$$

$$\Delta_{T,n} = \frac{1}{4} (\Delta_{L,n} - 2\Delta_{R,n}). \quad (93)$$

We then solve for the time-dependent perturbation $\delta\mathcal{F}_n$ to the flux \mathcal{F} at the stellar surface according to Eqn. 11 of Townsend (2003),

$$\frac{\delta\mathcal{F}_n}{\mathcal{F}} = \Delta_{R,n} \mathcal{R}_\ell + \Delta_{T,n} \mathcal{T}_\ell + \Delta_{g,n} \mathcal{G}_\ell, \quad \Rightarrow \quad \widetilde{\Delta m}_{\ell,n} = -10^6 \frac{2.5}{\ln 10} \frac{\delta\mathcal{F}}{\mathcal{F}}, \quad (94)$$

where $\widetilde{\Delta m}_{\ell,n}$ is the apparent magnitude fluctuation associated with eigenmode n in units of μmag . We use MSG (Townsend & Lopez 2023, version 1.1.2) to calculate the photometric intensity D-moment \mathcal{I}_ℓ and its partial derivatives (e.g., Eqn. 15 of Townsend (2003)). MSG uses literature grids to synthesize the stellar spectrum at each wavelength then applies an instrumental passband to create a realistic prediction for the intensity moments. We use the OSTAR2002 grid in our $15M_\odot$ and $40M_\odot$ calculations (Lanz & Hubeny 2003) and an extended version of the MSG demo grid for the $3M_\odot$ star (Castelli & Kurucz 2003). We use the TESS passband⁸ with the ‘Red’ filter from the SVO Filter Profile

⁸ The red noise observations presented in Figs. 2-3 of the main text from Bowman et al. (2020) are from TESS.

Table 4. Table of computed intensity moment relationships computed from MSG for each spherical harmonic degree. The $\ell = 0$ intensity moments normalized to the zero-point flux for the three models studied in this work are respectively $\mathcal{I}_0 = \{4.58 \times 10^{15}, 1.91 \times 10^{16}, 2.88 \times 10^{16}\}$ for the $\{3, 15, 40\} M_\odot$ stars. The first two columns report the spherical harmonic degree ℓ and the result of Eqn. 98 for that value of ℓ . The next three columns show the photometric moment ratios used in Eqns. 95–97 for the $3 M_\odot$ star, and the next two sets of three columns show the same data for the 15 and $40 M_\odot$ stars, respectively.

ℓ	\bar{Y}_ℓ	$\left(\frac{\mathcal{I}_\ell}{\mathcal{I}_0}\right)_3$	$\left(\frac{1}{\mathcal{I}_0} \frac{\partial \mathcal{I}_\ell}{\partial \ln T_{\text{eff}}}\right)_3$	$\left(\frac{1}{\mathcal{I}_0} \frac{\partial \mathcal{I}_\ell}{\partial \ln g}\right)_3$	$\left(\frac{\mathcal{I}_\ell}{\mathcal{I}_0}\right)_{15}$	$\left(\frac{1}{\mathcal{I}_0} \frac{\partial \mathcal{I}_\ell}{\partial \ln T_{\text{eff}}}\right)_{15}$	$\left(\frac{1}{\mathcal{I}_0} \frac{\partial \mathcal{I}_\ell}{\partial \ln g}\right)_{15}$	$\left(\frac{\mathcal{I}_\ell}{\mathcal{I}_0}\right)_{40}$	$\left(\frac{1}{\mathcal{I}_0} \frac{\partial \mathcal{I}_\ell}{\partial \ln T_{\text{eff}}}\right)_{40}$	$\left(\frac{1}{\mathcal{I}_0} \frac{\partial \mathcal{I}_\ell}{\partial \ln g}\right)_{40}$
1	0.132	6.8×10^{-1}	1.1	-4.1×10^{-3}	6.8×10^{-1}	1.2	-1.3×10^{-2}	6.8×10^{-1}	7.5×10^{-1}	-1.2×10^{-3}
2	0.129	2.8×10^{-1}	4.2×10^{-1}	-1.7×10^{-3}	2.7×10^{-1}	4.8×10^{-1}	-6.7×10^{-3}	2.7×10^{-1}	3.0×10^{-1}	-4.0×10^{-3}
3	0.126	2.3×10^{-2}	1.6×10^{-2}	-1.7×10^{-4}	1.6×10^{-2}	1.8×10^{-2}	-1.6×10^{-3}	1.4×10^{-2}	1.8×10^{-2}	-3.2×10^{-3}
4	0.125	-3.6×10^{-2}	-6.3×10^{-2}	2.3×10^{-4}	-3.8×10^{-2}	-7.4×10^{-2}	5.4×10^{-4}	-3.9×10^{-2}	-4.4×10^{-2}	-4.8×10^{-4}
5	0.123	-5.1×10^{-3}	-3.8×10^{-3}	5.2×10^{-5}	-3.7×10^{-3}	-5.6×10^{-3}	4.4×10^{-4}	-3.7×10^{-3}	-5.4×10^{-3}	9.5×10^{-4}
6	0.122	1.3×10^{-2}	2.3×10^{-2}	-7.8×10^{-5}	1.4×10^{-2}	2.7×10^{-2}	-1.2×10^{-4}	1.4×10^{-2}	1.6×10^{-2}	3.7×10^{-4}
7	0.122	1.9×10^{-3}	1.5×10^{-3}	-2.4×10^{-5}	1.4×10^{-3}	2.4×10^{-3}	-1.9×10^{-4}	1.5×10^{-3}	2.4×10^{-3}	-4.3×10^{-4}
8	0.121	-6.1×10^{-3}	-1.1×10^{-2}	3.7×10^{-5}	-6.7×10^{-3}	-1.3×10^{-2}	4.3×10^{-5}	-6.8×10^{-3}	-7.5×10^{-3}	-2.5×10^{-4}
9	0.120	-9.3×10^{-4}	-7.8×10^{-4}	1.5×10^{-5}	-7.2×10^{-4}	-1.4×10^{-3}	1.1×10^{-4}	-8.3×10^{-4}	-1.4×10^{-3}	2.3×10^{-4}
10	0.120	3.5×10^{-3}	6.6×10^{-3}	-2.0×10^{-5}	3.8×10^{-3}	7.5×10^{-3}	-1.4×10^{-5}	3.9×10^{-3}	4.2×10^{-3}	1.7×10^{-4}
11	0.119	5.2×10^{-4}	4.6×10^{-4}	-9.7×10^{-6}	4.2×10^{-4}	8.8×10^{-4}	-6.9×10^{-5}	5.1×10^{-4}	8.7×10^{-4}	-1.4×10^{-4}
12	0.119	-2.2×10^{-3}	-4.2×10^{-3}	1.2×10^{-5}	-2.4×10^{-3}	-4.7×10^{-3}	2.0×10^{-6}	-2.5×10^{-3}	-2.6×10^{-3}	-1.3×10^{-4}
13	0.119	-3.2×10^{-4}	-3.0×10^{-4}	6.7×10^{-6}	-2.7×10^{-4}	-6.0×10^{-4}	4.7×10^{-5}	-3.3×10^{-4}	-5.8×10^{-4}	9.1×10^{-5}
14	0.118	1.5×10^{-3}	2.8×10^{-3}	-7.4×10^{-6}	1.6×10^{-3}	3.2×10^{-3}	3.0×10^{-6}	1.7×10^{-3}	1.7×10^{-3}	9.6×10^{-5}
15	0.118	2.1×10^{-4}	2.0×10^{-4}	-4.9×10^{-6}	1.8×10^{-4}	4.3×10^{-4}	-3.4×10^{-5}	2.3×10^{-4}	4.1×10^{-4}	-6.3×10^{-5}

646 Service (Rodrigo & Solano 2020). The differential flux functions are defined in Eqns. 12–14 of Townsend (2003),

647

$$\mathcal{R}_\ell = (2 + \ell)(1 - \ell) \frac{\mathcal{I}_\ell}{\mathcal{I}_0} \bar{Y}_\ell \quad (95)$$

648

$$\mathcal{T}_\ell = \frac{1}{\mathcal{I}_0} \frac{\partial \mathcal{I}_\ell}{\partial \ln T_{\text{eff}}} \bar{Y}_\ell \quad (96)$$

649

$$\mathcal{G}_\ell = \frac{1}{\mathcal{I}_0} \frac{\partial \mathcal{I}_\ell}{\partial \ln g} \bar{Y}_\ell \quad (97)$$

650

651 To account for an arbitrary observing angle, we generalize our results by taking an appropriately weighted angle
652 average as in Eqn. 8 of Townsend (2002),

653

$$\bar{Y}_\ell = \frac{1}{2\ell + 1} \sum_{m=-\ell}^{\ell} \frac{1}{4\pi} \int_0^{2\pi} \int_0^\pi |Y_\ell^m(\Theta, \Phi)| \sin \Theta d\Theta d\Phi. \quad (98)$$

654 Values of the intensity moments, their partial derivatives, and \bar{Y}_ℓ used in this work for each star are presented in
655 table 4.

656 6.2. The transfer function

657 After calculating the surface photometric magnitude perturbation associated with each wave, we generate a transfer
658 function according to Eqn. 71 at each ℓ . Transfer functions for $\ell = [1, 2, 3]$ for each of our $3, 15$, and $40 M_\odot$ models
659 studied in this work are shown in Fig. 8. In order to retrieve the spectrum of photometric variability at the surface of
660 the star in μmag , we will multiply these transfer functions by the square root of the wave luminosity (Eqn. 74).

661 For comparison, we also show transfer functions for $10^6 s_1/c_p$ from the Wave Propagation simulation in the middle
662 panels of Fig. 8. We see that even though our Wave Propagation simulation captures 93% of the stellar radius and
663 99.99925% of the stellar mass, the signal at the surface of our simulation is quite different from that at the surface
664 of the star. In particular, the transfer function in our simulations has a low-frequency damping tail which occurs at
665 too high of a frequency compared to the full star, so low frequency waves are damped too heavily in our simulations

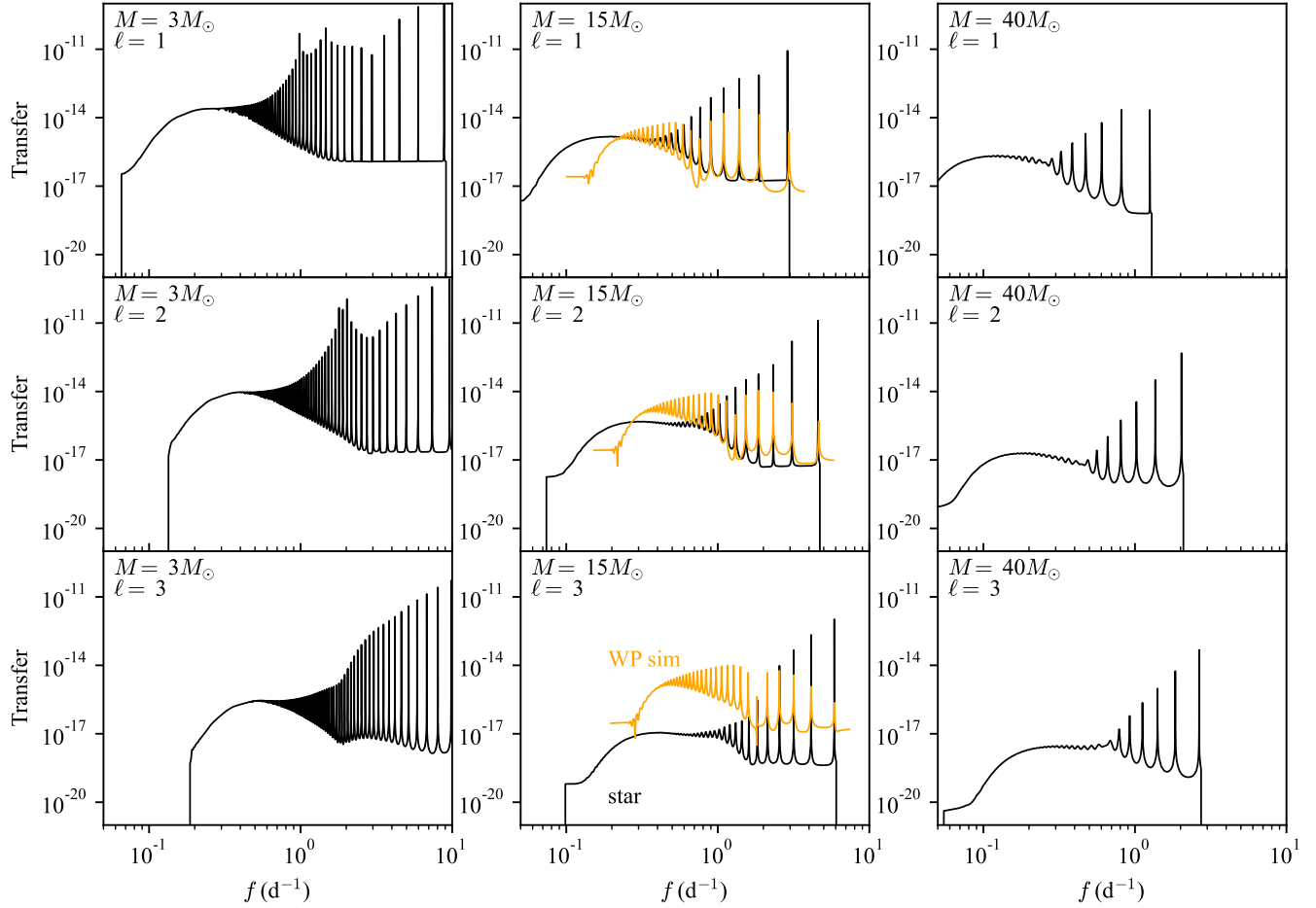


Figure 8. We plot the transfer functions for (top row) $\ell = 1$, (middle row) $\ell = 2$, and (bottom row) $\ell = 3$ for our (left column) $3M_{\odot}$, (middle column) $15M_{\odot}$, and (right column) $40M_{\odot}$ stars. Black lines show the transfer function for converting the square root of the gravity wave luminosity into photometric variability in μmag at the stellar photosphere. The orange lines in the middle columns show comparable transfer functions for the Wave Propagation simulation. As ℓ increases, the stellar transfer functions fall in amplitude compared to the simulation transfer functions; this occurs because the stellar transfer functions include wave cancellation and limb darkening effects which are incurred when observing a hemisphere for comparison with observations, while the simulation transfer functions do not.

666 compared to the star. Our simulation transfer functions do have high-frequency peaks at frequencies which are very
 667 close to the oscillation frequencies present in the real star, which makes sense as the bulk of the high-frequency wave
 668 cavity is deep in the star and these waves are evanescent near the surface. However, the quality factor of the wave peaks
 669 in our simulated transfer functions are much lower than they are for the full star due to the simulation diffusivities
 670 and excess damping from timestepping; we do not apply the timestepping correction laid out Sec. 5.2.1 to the GYRE
 671 eigenmodes when creating the transfer functions used in our predictions of the observable photometric variability.

672 Note that the transfer function for the star decreases sharply in magnitude as ℓ increases while the simulation
 673 transfer function does not. This occurs because when we use MSG to calculate $\tilde{\Delta m}_{\ell,n}$, we account for the effects of
 674 limb darkening and cancellation (Table 4); these effects result in smaller photometric variability perturbations from
 675 modes at high spherical harmonic degree. We do not include these in our simulations, where the transfer function
 676 gives the amplitude expected for the wave over the full 4π .

677 6.3. Synthesis of photometric variability spectra

678 We generate a transfer function according to Eqn. 70 and use it to filter the wave luminosity to predict the surface
 679 photometric variability for each spherical harmonic $\ell = [1, 15]$ according to Eqn. 71 and using the wave luminosity
 680 fits in Eqn. 74. We sample the synthesized variability in uniformly spaced frequency bins $\Delta f = 3.17 \times 10^{-8}$ Hz up

to $f_{\max} = 5.55 \times 10^{-4}$ Hz, corresponding to a year of observational data sampled every 30 minutes. We plot the magnitude contributions of each ℓ for each star in the left panels of Fig. 9. We plot partial quadrature sums of the total observed photometric variability for each star in the right panels of Fig. 9. The contributions of odd spherical harmonic degrees are shown as green lines, and the contributions of even spherical harmonic degrees are shown as purple lines. We find that the dominant contributions are from the $\ell = 1$ mode, and aside from that the even modes contribute more powerfully to the observed spectra than the odd modes, which experience more cancellation. In most transfer functions, we see a “tail” at low frequency where the transfer function begins to increase again. This “tail” is a numerical artifact which arises because the eigenfunction expansion breaks down for low frequencies for gravity waves of high radial order, making the transfer function calculation unreliable for low frequencies. We know that the transfer function should be falling off exponentially in this regime due to radiative diffusivity, so it is not a bad approximation to set it equal to zero here, which we do.

From the right-hand panels, we see that the majority of the observed signal is caused by the $\ell = 1$ contribution. At higher frequencies, the contributions of higher ℓ values increase the magnitude of the “tail” of the gravity wave signal. The main broad peak of the signal is therefore saturated by our inclusion of $\ell = [1, 15]$, but a small amount of power would continue to be added at high frequencies if we were to include all spherical harmonic degrees. We find that for $\ell > 15$, GYRE has trouble faithfully reconstructing the eigenfunctions, and so we are limited to the values of ℓ studied here.

698 6.4. Red noise fits to synthesized spectra

699 In Fig. 10, we show Lorentzian fits (orange lines) of the form,

$$700 \quad \alpha(\nu) = \frac{\alpha_0}{1 + \left(\frac{\nu}{\nu_{\text{char}}}\right)^{\gamma}}. \quad (99)$$

701 to our photometric magnitude predictions (black lines). Fits are made by-eye with the goal of having the fit describe
 702 the peak amplitude of the wave signal and to have the Lorentzian tail follow the tail of the photometric variability
 703 spectrum, ignoring the resonant peaks.

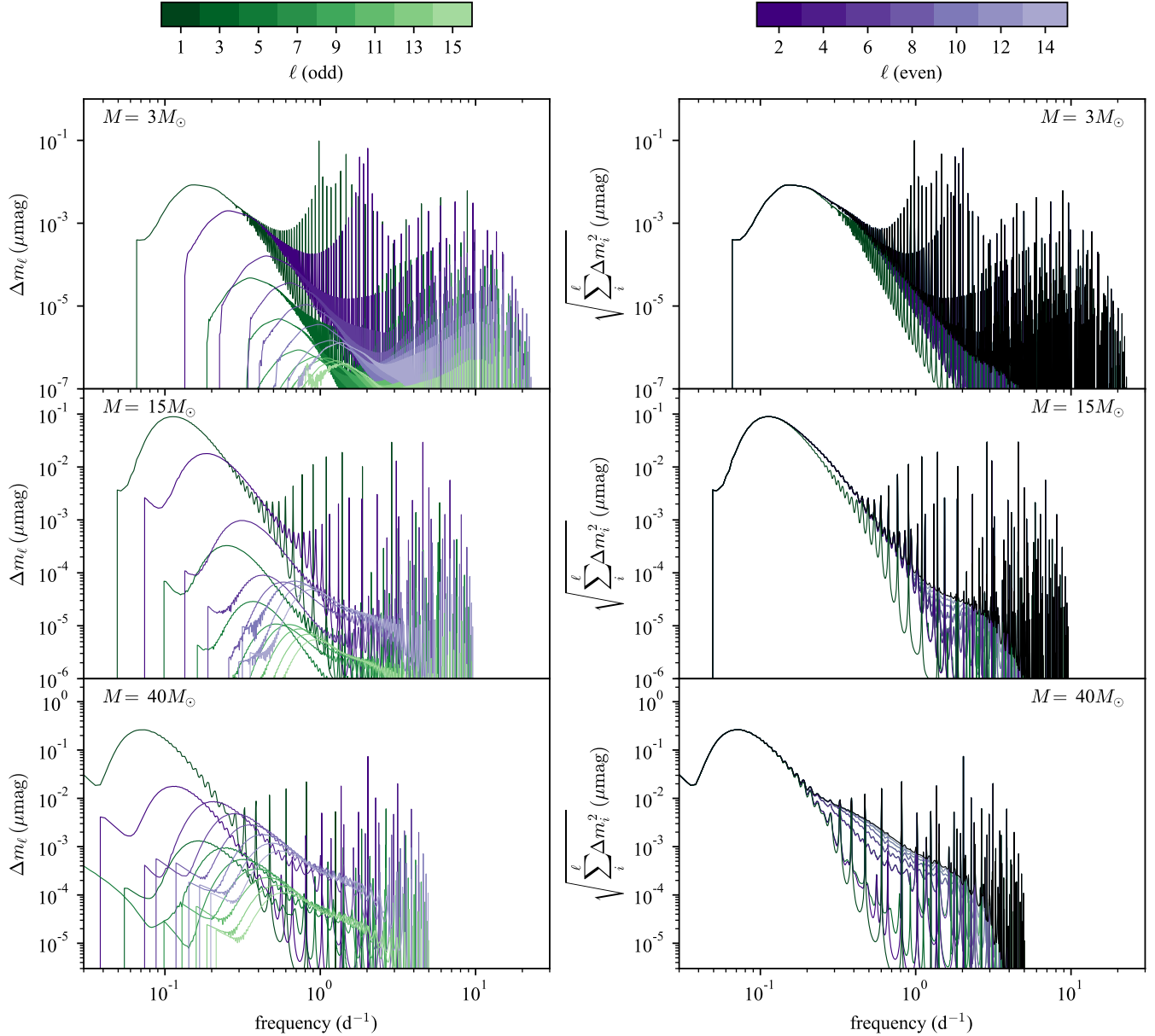


Figure 9. (Left panels) Shown are the photometric variability magnitude contributions for each spherical harmonic degree for the $3 M_{\odot}$ (top panel), $15 M_{\odot}$ (middle panel), and $40 M_{\odot}$ (bottom panel) stars. Odd ℓ lines are colored green and decrease in saturation as ℓ increases; even ℓ lines are similar but are colored purple. In the right panels, we correspondingly show partial quadrature sums of the full photometric variability signal from $\ell = 1$ to the ℓ value corresponding to the line color. The black lines are the sums over all plotted ℓ values and are the same lines as those plotted in the middle panel of Fig. 2 in the main text.

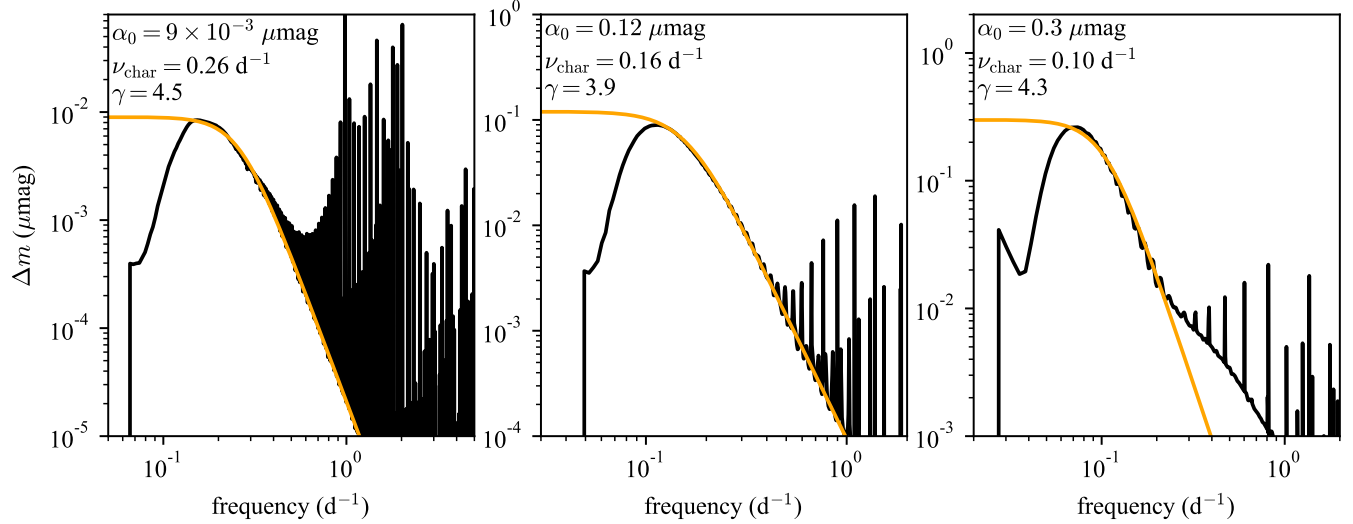


Figure 10. We plot the predicted photometric variability spectra of the $3 M_\odot$ (left), $15 M_\odot$ (middle), and $40 M_\odot$ (right) as black lines. We fit a Lorentzian profile as in Eqn. 99 by-eye to the turnover of these spectra at high frequency and overplot these as orange lines. The values used in the Lorentzian fit are reported in the upper left of each panel.

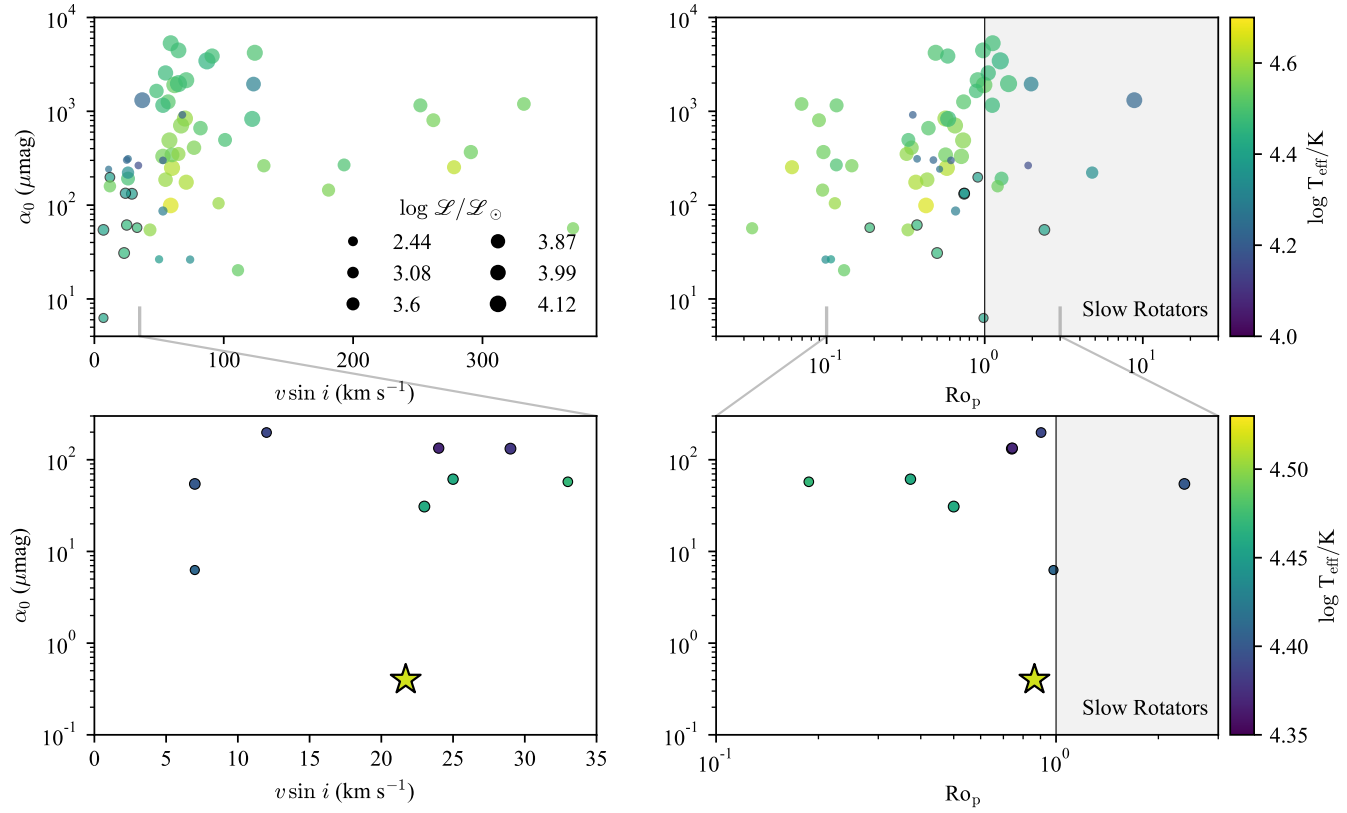


Figure 11. (Left panels) Red noise amplitude α_0 vs. projected rotational velocity $v \sin i$ (km / s). Data are colored by T_{eff} and the size of the markers corresponds to the spectroscopic luminosity \mathcal{L} of the star; data are retrieved from tables A1 and A2 of Bowman et al. (2020). (Right panels) Red noise amplitude α_0 vs projected Rossby number $\text{Ro}/\sin i$; marker color and size are determined in the same manner as in the left panel. When stars are at or above $\text{Ro} \sim 1$, rotation can affect convection but is not rapid enough to affect the waves themselves substantially. We term these stars “Slow Rotators”. The top panels show the full dataset; stars most similar in the $\mathcal{L} - T_{\text{eff}}$ plane to our fiducial star are outlined with black and are shown in the bottom panels. The bottom panels additionally contain a star point corresponding to the rotating simulation discussed in Section 7.2; note in the right panels that two stars lie on top of each other near $\text{Ro}_p \approx 0.8$ and $\alpha_0 \approx 200 \mu\text{mag}$.

7. THE EFFECTS OF ROTATION

7.1. Observations of stellar rotation and red noise

In the left panels of Fig. 11, we plot the amplitude of red noise versus $v \sin i$ of observed stars using data from table A2 of Bowman et al. (2020). Data points are colored by T_{eff} and the size of the points correspond to the spectroscopic luminosity \mathcal{L} . In the top panels, we plot all points from the Bowman et al. (2020) dataset, but we have discarded stars whose effective temperature and luminosity lie outside of the main sequence according to MESA stellar models from Jermyn et al. (2022a); this discards a few stars just to the left of the model ZAMS and all post-main sequence stars. The points with black outlines are the points with similar T_{eff} and \mathcal{L} to our fiducial $15 M_{\odot}$ star, and appear in Fig. 2 of the main manuscript. In the bottom panels of Fig. 11, we show zoomed views that focus just on the stars most similar to our fiducial star. We also include an estimate of the photometric variability from one rotating simulation, discussed in Section 7.2 and marked as a star.

The importance of rotation on convective motions depends on both the rotation rate of the star and the characteristic overturn timescale of the convective motions. This is quantified by the Rossby number⁹ (e.g., Aurnou et al. 2020),

$$\text{Ro} = \frac{U}{2\Omega L} = \frac{P_{\text{rot}}}{t_{\text{conv}}}, \quad (100)$$

⁹ We note that this value of Ro may not describe the aspect ratio of convective features well when $\text{Ro} < 1$ (Vasil et al. 2021).

where U is a characteristic convective velocity, L is a characteristic length scale, Ω is the stellar angular rotation frequency, and P_{rot} and t_{conv} are respectively the rotational period and convective timescales. For each star in the sample, we calculate a projected rotation period, $P_{\text{rot,p}} = 2\pi R_*/(v \sin i)$. We interpolate the convective turnover time of the core convection zone from the MESA models of Jermyn et al. (2022a) in \mathcal{L} - T_{eff} space and we determine t_{conv} for each star from the \mathcal{L} and T_{eff} . We calculate an approximate projected Rossby number for each star,

$$\text{Ro}_p = \frac{\text{Ro}}{\sin i} = \frac{P_{\text{rot,p}}}{t_{\text{conv}}}. \quad (101)$$

In the right panels of Fig. 11, we plot the magnitude of red noise vs. Ro_p . Here we assume rigid rotation when calculating Ro_p , but stars could be rotating differentially (Bowman 2020).

We find no clear correlation between projected rotational velocity and red noise amplitude. Even accounting for the convective overturn timescale via the Rossby number, there is no clear trend. We do note that the highest magnitude red noise fluctuations seem to occur on stars with moderately high Rossby number or moderately low $v \sin i$. If rotation were boosting convective wave excitation which were in turn causing red noise, we would expect to see a clear increase of α with increasing $v \sin i$, or likewise a clear decrease in α with increasing Ro_p .

It is important to note that $v \sin i$ contains a degeneracy between the stellar rotational velocity and the star's inclination angle. Augustson et al. (2020) theorize that rotation can boost the wave luminosity significantly, and we expect $v \sin i$ to be a robust indication of whether rotationally-boosted waves could be viewed on a rotating star. If the star is a slow rotator, then $v \sin i$ will be small and our non-rotating theory here should apply. If the star is a rapid rotator, its waves will be confined to the equator. If the waves are equatorially trapped, viewing the star from a polar angle (small $\sin i$) will lead to lower wave photometric variability than viewing the star from an equatorial angle ($\sin i \sim 1$).

7.2. A $15M_{\odot}$ simulation with $P_{\text{rot}} = 10$

All stars rotate, so it is important to understand how rotation affects our predictions for the photometric variability of massive stars. There are at least two basic ways that rotation can affect gravity waves generated by core convection: by affecting the character of the convection in the core, or by affecting the waves themselves. Rotation affects convection in the core when the Rossby number $\text{Ro} \sim 1$ or smaller. In rotating convection, convective structures align with the rotation axis forming columns and gaining significant anisotropy and organization (c.f., Aurnou et al. 2020; Featherstone & Hindman 2016). This can happen even when the rotation frequency is much lower than the wave frequencies, so convection can change character despite the waves being nearly the same as in the non-rotating case. A stably stratified region under the influence of rotation exhibits both gravito-inertial waves and inertial waves (Mathis et al. 2014), so rotation strongly affects the frequencies and structure of oscillation modes with frequencies $\lesssim 2P_{\text{rot}}^{-1}$. Properly accounting for rotation in eigenvalue solves and the construction of the transfer function is a difficult task which is beyond the scope of this work.

However, most of the features of the transfer functions for our fiducial $15 M_{\odot}$ star occur at frequencies greater than 0.2 d^{-1} , so for rotation periods $P_{\text{rot}} \geq 10 \text{ d}$, using the transfer functions built based on non-rotating modes is a decent first approximation. From the bottom panels of Fig. 11, we see that stars similar to our fiducial star have $v \sin i \sim 5 - 30 \text{ km s}^{-1}$, and these similar stars have a median $v \sin i = 24 \text{ km s}^{-1}$. Our fiducial $15 M_{\odot}$ has $R_* = 4.289 R_{\odot}$; therefore a 10-day rotation period produces a surface equatorial rotation velocity of $v = 21.7 \text{ km s}^{-1}$, which is similar to the median $v \sin i$ in the limited sample of observed stars shown in Fig. 2 of the main manuscript. We therefore run one Wave Generation simulation of our fiducial model with a rotation period of 10 days. The goal of this simulation is not to study wave generation in a rapidly-rotating star, but rather to determine if a modest rotation rate drastically changes the convection generation of waves.

We calculate the convective timescale of our fiducial model according to Eqn. 20 of Jermyn et al. (2022a),

$$t_{\text{conv}} = \int_{\text{CZ}} \frac{dr}{v_c}, \quad (102)$$

where v_c is the MLT convective velocity, and find $t_{\text{conv}} = 14.75 \text{ d}$. Taking the average value $|\sin i| = \pi/4$, the approximate projected Rossby number of this simulation is $\text{Ro}_p = P_{\text{rot}}/(t_{\text{conv}} |\sin i|) = 0.91$. In the rotating simulation, the realized average velocity in the core convection zone is $7.94 \times 10^4 \text{ cm s}^{-1}$ (see Table 3); this velocity value is larger than in the non-rotating case because a differential rotation that is strong relative to the convective perturbations is

established in the azimuthal velocity. The velocity fluctuations around the differential rotation are of order 5.5×10^4 cm s $^{-1}$, commensurate with the nonrotating velocities and closely matching the MLT estimate for the velocity of 6.68×10^4 cm s $^{-1}$ given in Table 2; therefore estimating this simulation to have $\text{Ro}_p \approx 1$ is a reasonable approximation. The convective flows in this simulation are therefore influenced by rotation, but are not strongly constrained by it.

We display volume visualizations of the radial velocity of the rotating simulation and the comparison nonrotating simulation in Fig. 12. Note that in the nonrotating simulation (bottom panels), the convective flows predominantly form a large dipole flow; this flow migrates around the simulation over time, and the regions of most intense wave generation occur near the impacting site of the dipole and shear regions of the return flow (Herwig et al. 2023). In the rotating simulation, there is no dominant dipole flow; rather, the convective structures are elongated along the rotation axis and swept azimuthally by a strong differential rotation. In the rotating simulations, the wave generation seems to primarily be located near the pole. We refer the reader to the animated version of Fig. 12, where these phenomena are more clear than in a static image.

We now compare the wave luminosity of the rotating and nonrotating simulations in the top four panels of Fig. 13. We examine the wave luminosities for $\ell = \{1, 2\}$ and for $f = \{0.4, 0.8\}$ d $^{-1}$. Despite the different flow morphologies displayed in Fig. 12, we find that the wave luminosity spectra in the rotating simulation can still be described by a $f^{-6.5} k_h^4$ powerlaw (Lecoanet & Quataert 2013), but the rotating simulation has a slightly higher wave luminosity. We approximate the wave luminosity spectrum in the rotating simulation as

$$L_w = (3 \times 10^{-10} \text{ erg s}^{-1}) \left(\frac{f}{\text{Hz}} \right)^{-6.5} k_h^4, \quad (103)$$

with $k_h = \sqrt{\ell(\ell+1)}$; this fit is shown by the black line in the top four panels of Fig. 13 and is a factor of 13 larger than the nonrotating wave flux displayed in Eqn. 74.

We next approximate the surface variability of the rotating simulation. For convenience, we use the nonrotating transfer functions computed in Sec. 6; this might be a decent approximation if the stellar eigenmodes are only weakly modified by rotation, although it does not account for rotational splitting (Aerts et al. 2010, section 1.4.3), which would serve to reduce the amplitude of wave peaks in the frequency spectrum. The gravity waves which are most strongly affected by rotation have $f < 2P_{\text{rot}}^{-1}$; we do not observe many waves at $\ell \geq 2$ at those low frequencies in our rotating simulation (Fig. 13). We produce a photometric variability spectrum using the nonrotating transfer function (Fig. 8, middle panels) and the wave luminosity fit from the rotating simulation (Eqn. 103), and we compare this spectrum and the nonrotating spectrum in the bottom left panel of Fig. 13. As expected, the increase in the wave luminosity by about an order of magnitude shifts the photometric variability upwards by about half an order of magnitude, but the surface magnitude fluctuations are still very small, less than $0.5 \mu\text{mag}$. In the bottom right panel of Fig. 13, we plot a Lorentzian fit to this spectrum; this is the fit used to determine the α_0 -value of the rotating simulation in the bottom panels of Fig. 11.

In summary, we find that a moderate rotation is able to modestly boost the wave luminosity, but not to the point where the photometric variability is observable. Critically, we find that this conclusion holds even when the core convection itself is substantially affected, changing from dipole dominated in the non-rotating case to columnar convection in the $\text{Ro} \sim 1$ case. This gives us substantial confidence in our overall findings, that convectively driven waves are not the source of red noise photometric variability, for moderately rotating stars.

Many stars rotate more rapidly than the star that we simulate, and since rotation can boost the wave luminosity it is plausible that photometric variability due to convectively-driven gravity waves may reach observable magnitudes in very rapidly rotating stars. Future work should determine how to properly build transfer functions from rotating eigenvalues and eigenvectors, and should also understand how the wave luminosity varies with decreasing Ro .

While red noise is ubiquitous (Bowman et al. 2019), not all stars are rapid rotators. The low amplitude that we predict in our modestly rotating and nonrotating simulations rule out gravity waves driven by core convection as the source of this ubiquitous signal which is present both in very slow and very rapid rotators (Fig. 11, upper right panel). On the other hand, the observed insensitivity of red noise amplitude with stellar rotational velocity is expected if subsurface convection is the source of red noise, since the near-surface convective regions in OB stars are always in the regime of $\text{Ro} > 1$ (Cantiello et al. 2021; Jermyn et al. 2022a).

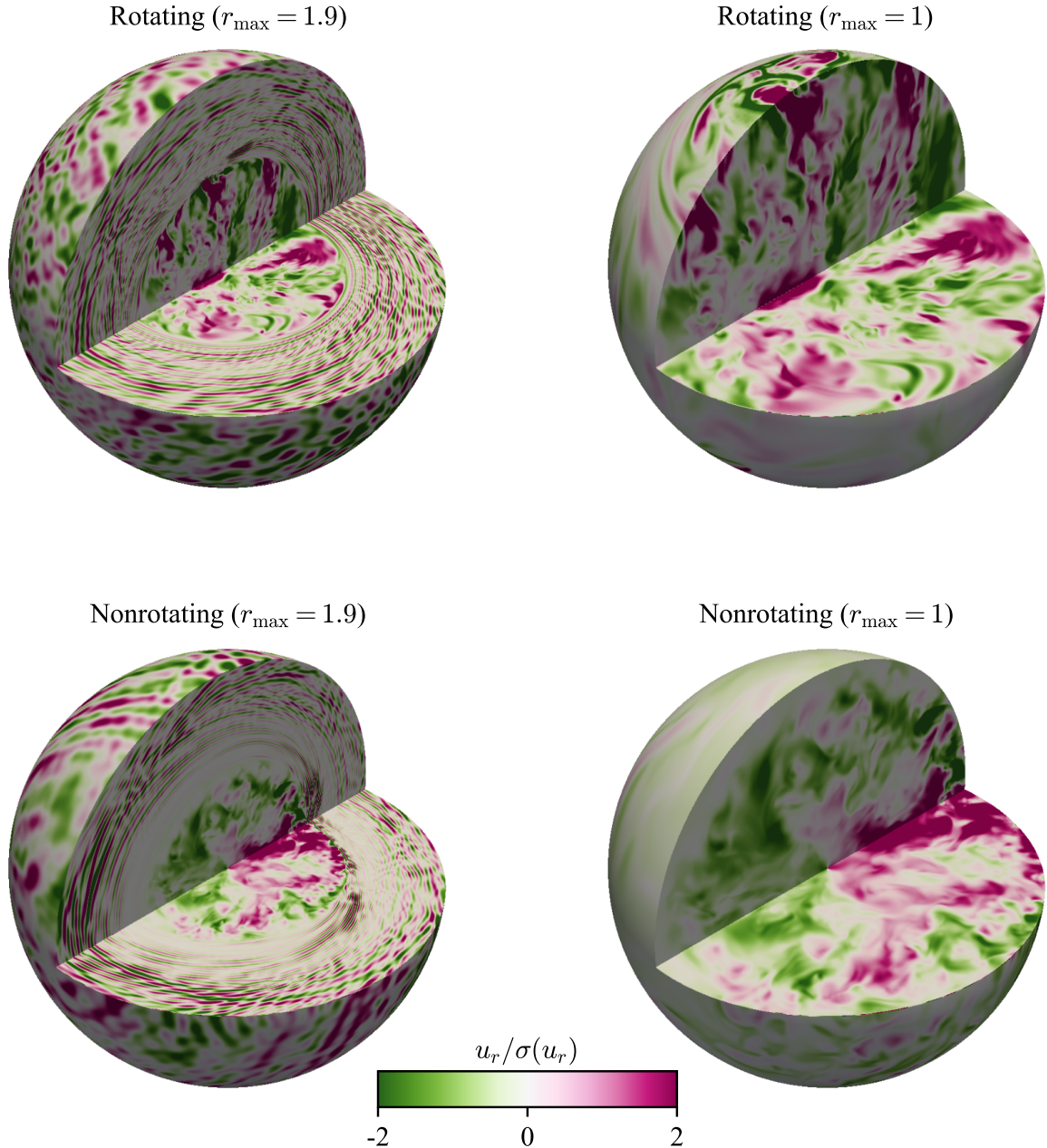


Figure 12. (Top panels) Volume visualizations of the rotating simulation including (left panel) 95% of the simulation domain and (right panel) 50% of the simulation domain; the right panel focuses on the convection zone while the left panel shows the dynamics throughout the simulation. Bottom panels are as in the top panels, but for the nonrotating case. As in the middle panel of Fig. 1 of the main manuscript, the plotted field is the radial velocity normalized by the standard deviation of the radial velocity at each radius. This figure was created using `PyVista` version 0.37.0 (Sullivan & Kaszynski 2019). An animated version of this still image can be found online in supplemental movie `15msol_rotating_and_nonrotating.mp4`.

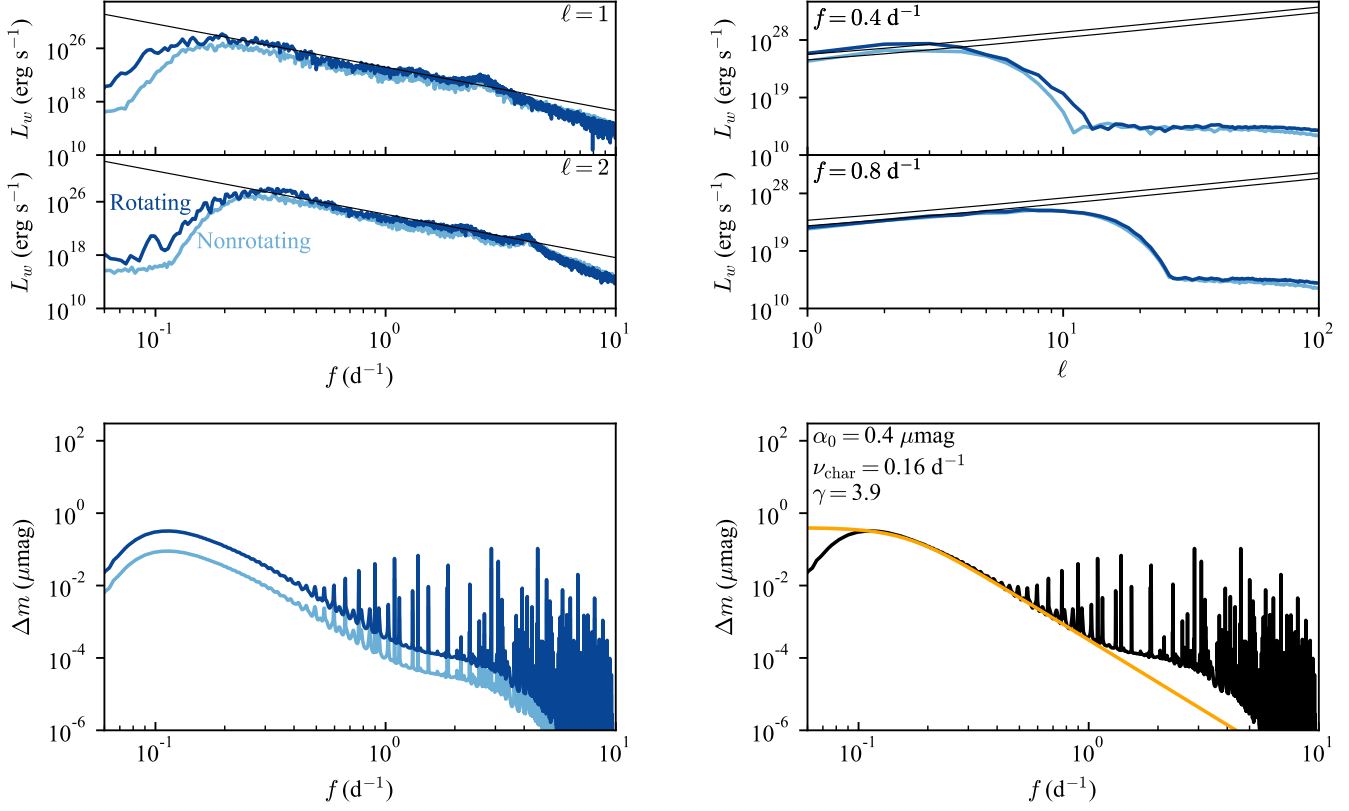


Figure 13. (Top four panels) The wave luminosity as in Fig. 3, but here we compare the wave luminosity of the rotating and nonrotating simulations of the $15 M_\odot$ star. The black line shows the fit from Eqn. 103. (Bottom left panel) Summed photometric variability spectra, as shown in Fig. 2 of the main text, here for the rotating and nonrotating $15 M_\odot$ simulations. (Bottom right panel) Red noise fit, as in Fig. 10, but here for the rotationally-boosted variability spectrum shown in the bottom left panel.

8. PROPERTIES OF THERMALLY DAMPED, ANELASTIC, INTERNAL GRAVITY WAVES

In this paper, we aim to study the properties of gravity waves including all of the most important physics. Therefore, we use wave polarization relations and dispersion relations which include the effects of the stellar density stratification and thermal diffusivity in our transfer function derivation in Section 3. The anelastic approximation is an ideal approximation to make in deriving these wave properties, and the linearized anelastic equations of motion are (Brown et al. 2012)

$$\nabla \cdot \mathbf{u} - u_r H_\rho^{-1} = 0, \quad (104)$$

$$\partial_t \mathbf{u} + \nabla \varpi + \frac{s_1}{c_p} \mathbf{g} = 0, \quad (105)$$

$$\partial_t s_1 + \mathbf{u} \cdot \nabla s_0 + \frac{1}{\rho_0 T_0} \nabla \cdot (-\kappa_{\text{rad}} \nabla T_1) = 0. \quad (106)$$

Here, the inverse density scale height is $H_\rho^{-1} = -\partial_r \ln \rho_0$, the gravitational acceleration is $\mathbf{g} = -g \hat{\mathbf{e}}_r$, the reduced pressure is $\varpi = P_1/\rho_0$, and subscripts “0” refer to the background stellar structure while subscripts “1” refer to the waves. For simplicity in writing the diffusion term, we will take $T_1 \sim T_0 s_1/c_p$ and we will assume that gradients in the radiative diffusivity $\chi_{\text{rad}} = \kappa_{\text{rad}} T_0/c_P$ are small compared to those in T_1 so that we can rewrite Eqn. 106 as

$$\partial_t s_1 + \mathbf{u} \cdot \nabla s_0 - \chi_{\text{rad}} \nabla^2 s_1 = 0. \quad (107)$$

8.1. Dispersion and polarization relations

For simplicity in deriving the polarization and dispersion relations, we will assume that the angular dependence of waves can be expressed using spin-weighted spherical harmonics and that the radial and temporal dependence can be expressed using exponentials with complex wavenumber \tilde{k}_r and complex angular frequency ω_n ,

$$u_{r,\ell}(r, \theta, \phi, t) = U_r Y_\ell(\theta, \phi) e^{-i\omega_n t + i\tilde{k}_r r}, \quad (108)$$

where U_r is the wave amplitude. We will approximate, $\nabla = \nabla_r \hat{\mathbf{e}}_r + \nabla_\phi \hat{\mathbf{e}}_\phi + \nabla_\theta \hat{\mathbf{e}}_\theta \approx \nabla_r + \nabla_h \approx i(\tilde{k}_r \hat{\mathbf{e}}_r + k_h \hat{\mathbf{e}}_h)$, where $\hat{\mathbf{e}}_h$ is a vector perpendicular to the radial direction, and we take $k_h = \sqrt{\ell(\ell+1)}/r$, and we decompose $\mathbf{u} = u_r \hat{\mathbf{e}}_r + u_h \hat{\mathbf{e}}_h$. The wave equations are

$$ik_h u_h + (i\tilde{k}_r - H_\rho) u_r = 0, \quad (109)$$

$$-i\omega_n u_r + ik_r \varpi - \frac{s_1}{c_p} g = 0, \quad (110)$$

$$-\omega_n u_h + k_h \varpi = 0, \quad (111)$$

$$\left(-i\omega_n + (k_h^2 + \tilde{k}_r^2) \chi_{\text{rad}} \right) s_1 + u_r \partial_r s_0 = 0, \quad (112)$$

The polarization relations, which express all perturbation variables in terms of u_r , are

$$u_h = -\frac{(\tilde{k}_r + iH_\rho)}{k_h} u_r, \quad (113)$$

$$\varpi = \frac{\omega_n}{k_h} u_h = -\frac{\omega_n}{k_h^2} (\tilde{k}_r + iH_\rho) u_r, \quad (114)$$

$$s_1 = \frac{\partial_r s_0}{\left(i\omega_n - (k_h^2 + \tilde{k}_r^2) \chi_{\text{rad}} \right)} u_r. \quad (115)$$

The dispersion relation is

$$-ik_h^2 N^2 + (-\omega_n [\tilde{k}_r^2 + k_h^2] - i\omega_n H_\rho^{-1} \tilde{k}_r) \left(-i\omega_n + \chi_{\text{rad}} [\tilde{k}_r^2 + k_h^2] \right) = 0, \quad (116)$$

where $N^2 = (g/c_p) \partial_r s_0$. In the limit that $H_\rho^{-1} = 0$ and $\chi_{\text{rad}} = 0$, this reduces to the classic gravity wave dispersion relation,

$$\omega_n^2 = N^2 \frac{k_h^2}{\tilde{k}_r^2 + k_h^2}. \quad (117)$$

854 For simplicity we assume that $H_\rho \tilde{k}_r \ll \tilde{k}_r^2 + k_h^2$ which allows us to obtain an equation which is quadratic in \tilde{k}_r^2 ,

$$855 \quad (ik_h^2(\omega_n^2 + N^2) - \omega_n \chi_{\text{rad}} k_h^4) + \tilde{k}_r^2 (i\omega_n^2 - 2\omega_n \chi_{\text{rad}} k_h^2) - \tilde{k}_r^4 (\omega_n \chi_{\text{rad}}) = 0. \quad (118)$$

856 This equation has four solutions for \tilde{k}_r ; as in Eqn. 12 of Lecoanet et al. (2015), we choose the solution where $\Re\{\tilde{k}_r\} < 0$,
 857 corresponding to upward propagating waves and $\Im\{\tilde{k}_r\} < 0$, corresponding to damped waves. Given a known k_h and
 858 ω_n for a wave, the radial wavenumber of a wave is

$$859 \quad \tilde{k}_r = \frac{(-1)^{3/4}}{\sqrt{2}} \sqrt{-2ik_h^2 - \frac{\omega}{\chi_{\text{rad}}} + \frac{\sqrt{\omega^3 + 4ik_h^2 \chi_{\text{rad}} N^2}}{\chi_{\text{rad}} \sqrt{\omega}}}. \quad (119)$$

860 The “optical depth” of a wave (see e.g., Shiode et al. 2013, Eqn. 7) can be found by radially integrating $\Im\{\tilde{k}_r\}$ from
 861 the excitation radius to the surface; waves with large optical depths are heavily damped. The radial wavenumber
 862 (characteristic oscillation inverse length scale) is the real component $k_r = \Re\{\tilde{k}_r\}$.

863 We use Eqns. 114 and 119 in Section 3.4.1 when we derive the transfer function.

REFERENCES

- 865 Aerts, C., Christensen-Dalsgaard, J., & Kurtz, D. W. 2010,
 866 Asteroseismology, doi: [10.1007/978-1-4020-5803-5](https://doi.org/10.1007/978-1-4020-5803-5)
- 867 Anders, E. H., & Brown, B. P. 2017, Physical Review
 868 Fluids, 2, 083501, doi: [10.1103/PhysRevFluids.2.083501](https://doi.org/10.1103/PhysRevFluids.2.083501)
- 869 Anders, E. H., Lecoanet, D., Cantiello, M., et al. 2023,
 870 Supplemental Data and Materials for "The photometric
 871 variability of massive stars due to gravity waves", 1.0,
 872 Zenodo, doi: [10.5281/zenodo.7764998](https://doi.org/10.5281/zenodo.7764998)
- 873 Angulo, C., Arnould, M., Rayet, M., et al. 1999, NuPhA,
 874 656, 3, doi: [10.1016/S0375-9474\(99\)00030-5](https://doi.org/10.1016/S0375-9474(99)00030-5)
- 875 Augustson, K. C., Mathis, S., & Astoul, A. 2020, ApJ, 903,
 876 90, doi: [10.3847/1538-4357/abba1c](https://doi.org/10.3847/1538-4357/abba1c)
- 877 Aurnou, J. M., Horn, S., & Julien, K. 2020, Physical
 878 Review Research, 2, 043115,
 879 doi: [10.1103/PhysRevResearch.2.043115](https://doi.org/10.1103/PhysRevResearch.2.043115)
- 880 Blouin, S., Shaffer, N. R., Saumon, D., & Starrett, C. E.
 881 2020, ApJ, 899, 46, doi: [10.3847/1538-4357/ab9e75](https://doi.org/10.3847/1538-4357/ab9e75)
- 882 Bowman, D. M. 2020, Frontiers in Astronomy and Space
 883 Sciences, 7, doi: [10.3389/fspas.2020.578584](https://doi.org/10.3389/fspas.2020.578584)
- 884 Bowman, D. M., Burssens, S., Simón-Díaz, S., et al. 2020,
 885 A&A, 640, A36, doi: [10.1051/0004-6361/202038224](https://doi.org/10.1051/0004-6361/202038224)
- 886 Bowman, D. M., Burssens, S., Pedersen, M. G., et al. 2019,
 887 Nature Astronomy, 3, 760,
 888 doi: [10.1038/s41550-019-0768-1](https://doi.org/10.1038/s41550-019-0768-1)
- 889 Boyd, J. P. 2001, Chebyshev and Fourier Spectral Methods
- 890 Brown, B. P., Vasil, G. M., & Zweibel, E. G. 2012, ApJ,
 891 756, 109, doi: [10.1088/0004-637X/756/2/109](https://doi.org/10.1088/0004-637X/756/2/109)
- 892 Burns, K. J., Vasil, G. M., Oishi, J. S., Lecoanet, D., &
 893 Brown, B. P. 2020, Physical Review Research, 2, 023068,
 894 doi: [10.1103/PhysRevResearch.2.023068](https://doi.org/10.1103/PhysRevResearch.2.023068)
- 895 Cantiello, M., Lecoanet, D., Jermyn, A. S., & Grassitelli, L.
 896 2021, ApJ, 915, 112, doi: [10.3847/1538-4357/ac03b0](https://doi.org/10.3847/1538-4357/ac03b0)
- 897 Cassisi, S., Potekhin, A. Y., Pietrinferni, A., Catelan, M., &
 898 Salaris, M. 2007, ApJ, 661, 1094, doi: [10.1086/516819](https://doi.org/10.1086/516819)
- 899 Castelli, F., & Kurucz, R. L. 2003, in Modelling of Stellar
 900 Atmospheres, ed. N. Piskunov, W. W. Weiss, & D. F.
 901 Gray, Vol. 210, A20,
 902 doi: [10.48550/arXiv.astro-ph/0405087](https://doi.org/10.48550/arXiv.astro-ph/0405087)
- 903 Chugunov, A. I., Dewitt, H. E., & Yakovlev, D. G. 2007,
 904 PhRvD, 76, 025028, doi: [10.1103/PhysRevD.76.025028](https://doi.org/10.1103/PhysRevD.76.025028)
- 905 Couston, L.-A., Lecoanet, D., Favier, B., & Le Bars, M.
 906 2018, Journal of Fluid Mechanics, 854, R3,
 907 doi: [10.1017/jfm.2018.669](https://doi.org/10.1017/jfm.2018.669)
- 908 Cyburt, R. H., Amthor, A. M., Ferguson, R., et al. 2010,
 909 ApJS, 189, 240, doi: [10.1088/0067-0049/189/1/240](https://doi.org/10.1088/0067-0049/189/1/240)
- 910 Dziembowski, W. 1977, AcA, 27, 203
- 911 Featherstone, N. A., & Hindman, B. W. 2016, ApJL, 830,
 912 L15, doi: [10.3847/2041-8205/830/1/L15](https://doi.org/10.3847/2041-8205/830/1/L15)
- 913 Ferguson, J. W., Alexander, D. R., Allard, F., et al. 2005,
 914 ApJ, 623, 585, doi: [10.1086/428642](https://doi.org/10.1086/428642)
- 915 Fuller, G. M., Fowler, W. A., & Newman, M. J. 1985, ApJ,
 916 293, 1, doi: [10.1086/163208](https://doi.org/10.1086/163208)
- 917 Goldreich, P., & Kumar, P. 1990, ApJ, 363, 694,
 918 doi: [10.1086/169376](https://doi.org/10.1086/169376)
- 919 Herwig, F., Woodward, P. R., Mao, H., et al. 2023, arXiv
 920 e-prints, arXiv:2303.05495,
 921 doi: [10.48550/arXiv.2303.05495](https://doi.org/10.48550/arXiv.2303.05495)
- 922 Howell, S. B., Sobeck, C., Haas, M., et al. 2014, PASP, 126,
 923 398, doi: [10.1086/676406](https://doi.org/10.1086/676406)
- 924 Iglesias, C. A., & Rogers, F. J. 1993, ApJ, 412, 752,
 925 doi: [10.1086/172958](https://doi.org/10.1086/172958)
- 926 —. 1996, ApJ, 464, 943, doi: [10.1086/177381](https://doi.org/10.1086/177381)
- 927 Irwin, A. W. 2004, The FreeEOS Code for Calculating the
 928 Equation of State for Stellar Interiors.
<http://freeeos.sourceforge.net/>
- 929 Itoh, N., Hayashi, H., Nishikawa, A., & Kohyama, Y. 1996,
 930 ApJS, 102, 411, doi: [10.1086/192264](https://doi.org/10.1086/192264)
- 931 Jermyn, A. S., Anders, E. H., Lecoanet, D., & Cantiello, M.
 932 2022a, ApJS, 262, 19, doi: [10.3847/1538-4365/ac7cee](https://doi.org/10.3847/1538-4365/ac7cee)
- 933 Jermyn, A. S., Schwab, J., Bauer, E., Timmes, F. X., &
 934 Potekhin, A. Y. 2021, ApJ, 913, 72,
 935 doi: [10.3847/1538-4357/abf48e](https://doi.org/10.3847/1538-4357/abf48e)
- 936 Jermyn, A. S., Bauer, E. B., Schwab, J., et al. 2022b, arXiv
 937 e-prints, arXiv:2208.03651,
 938 doi: [10.48550/arXiv.2208.03651](https://doi.org/10.48550/arXiv.2208.03651)
- 939 Landau, L. D., & Lifshitz, E. M. 1987, Fluid Mechanics
- 940 Langanke, K., & Martínez-Pinedo, G. 2000, Nuclear
 941 Physics A, 673, 481, doi: [10.1016/S0375-9474\(00\)00131-7](https://doi.org/10.1016/S0375-9474(00)00131-7)
- 942 Lanz, T., & Hubeny, I. 2003, ApJS, 146, 417,
 943 doi: [10.1086/374373](https://doi.org/10.1086/374373)
- 944 Le Saux, A., Guillet, T., Baraffe, I., et al. 2022, A&A, 660,
 945 A51, doi: [10.1051/0004-6361/202142569](https://doi.org/10.1051/0004-6361/202142569)
- 946 Lecoanet, D., Cantiello, M., Anders, E. H., et al. 2021,
 947 MNRAS, 508, 132, doi: [10.1093/mnras/stab2524](https://doi.org/10.1093/mnras/stab2524)
- 948 Lecoanet, D., Le Bars, M., Burns, K. J., et al. 2015,
 949 PhRvE, 91, 063016, doi: [10.1103/PhysRevE.91.063016](https://doi.org/10.1103/PhysRevE.91.063016)
- 950 Lecoanet, D., & Quataert, E. 2013, MNRAS, 430, 2363,
 951 doi: [10.1093/mnras/stt055](https://doi.org/10.1093/mnras/stt055)
- 952 Lecoanet, D., Vasil, G. M., Burns, K. J., Brown, B. P., &
 953 Oishi, J. S. 2019, Journal of Computational Physics: X, 3,
 954 100012, doi: <https://doi.org/10.1016/j.jcpx.2019.100012>

- 956 Lecoanet, D., Cantiello, M., Quataert, E., et al. 2019,
 957 ApJL, 886, L15, doi: [10.3847/2041-8213/ab5446](https://doi.org/10.3847/2041-8213/ab5446)
- 958 Mathis, S., Neiner, C., & Tran Minh, N. 2014, A&A, 565,
 959 A47, doi: [10.1051/0004-6361/201321830](https://doi.org/10.1051/0004-6361/201321830)
- 960 Oda, T., Hino, M., Muto, K., Takahara, M., & Sato, K.
 961 1994, Atomic Data and Nuclear Data Tables, 56, 231,
 962 doi: [10.1006/adnd.1994.1007](https://doi.org/10.1006/adnd.1994.1007)
- 963 Oishi, J., Burns, K., Clark, S., et al. 2021, The Journal of
 964 Open Source Software, 6, 3079, doi: [10.21105/joss.03079](https://doi.org/10.21105/joss.03079)
- 965 Paxton, B., Bildsten, L., Dotter, A., et al. 2011, ApJS, 192,
 966 3, doi: [10.1088/0067-0049/192/1/3](https://doi.org/10.1088/0067-0049/192/1/3)
- 967 Paxton, B., Cantiello, M., Arras, P., et al. 2013, ApJS, 208,
 968 4, doi: [10.1088/0067-0049/208/1/4](https://doi.org/10.1088/0067-0049/208/1/4)
- 969 Paxton, B., Marchant, P., Schwab, J., et al. 2015, ApJS,
 970 220, 15, doi: [10.1088/0067-0049/220/1/15](https://doi.org/10.1088/0067-0049/220/1/15)
- 971 Paxton, B., Schwab, J., Bauer, E. B., et al. 2018, ApJS,
 972 234, 34, doi: [10.3847/1538-4365/aaa5a8](https://doi.org/10.3847/1538-4365/aaa5a8)
- 973 Paxton, B., Smolec, R., Schwab, J., et al. 2019, ApJS, 243,
 974 10, doi: [10.3847/1538-4365/ab2241](https://doi.org/10.3847/1538-4365/ab2241)
- 975 Potekhin, A. Y., & Chabrier, G. 2010, Contributions to
 976 Plasma Physics, 50, 82, doi: [10.1002/ctpp.201010017](https://doi.org/10.1002/ctpp.201010017)
- 977 Poutanen, J. 2017, ApJ, 835, 119,
 978 doi: [10.3847/1538-4357/835/2/119](https://doi.org/10.3847/1538-4357/835/2/119)
- 979 Ricker, G. R., Winn, J. N., Vanderspek, R., et al. 2014,
 980 Journal of Astronomical Telescopes, Instruments, and
 981 Systems, 1, 014003, doi: [10.1117/1.JATIS.1.1.014003](https://doi.org/10.1117/1.JATIS.1.1.014003)
- 982 Rodrigo, C., & Solano, E. 2020, in XIV.0 Scientific Meeting
 983 (virtual) of the Spanish Astronomical Society, 182
- 984 Rogers, F. J., & Nayfonov, A. 2002, ApJ, 576, 1064,
 985 doi: [10.1086/341894](https://doi.org/10.1086/341894)
- 986 Rogers, T. M., Lin, D. N. C., McElwaine, J. N., & Lau,
 987 H. H. B. 2013, ApJ, 772, 21,
 988 doi: [10.1088/0004-637X/772/1/21](https://doi.org/10.1088/0004-637X/772/1/21)
- 989 Saumon, D., Chabrier, G., & van Horn, H. M. 1995, ApJS,
 990 99, 713, doi: [10.1086/192204](https://doi.org/10.1086/192204)
- 991 Shiode, J. H., Quataert, E., Cantiello, M., & Bildsten, L.
 992 2013, MNRAS, 430, 1736, doi: [10.1093/mnras/sts719](https://doi.org/10.1093/mnras/sts719)
- 993 Sullivan, C., & Kaszynski, A. 2019, The Journal of Open
 994 Source Software, 4, 1450, doi: [10.21105/joss.01450](https://doi.org/10.21105/joss.01450)
- 995 Timmes, F. X., & Swesty, F. D. 2000, ApJS, 126, 501,
 996 doi: [10.1086/313304](https://doi.org/10.1086/313304)
- 997 Townsend, R., & Lopez, A. 2023, Journal of Open Source
 998 Software, 8, 4602, doi: [10.21105/joss.04602](https://doi.org/10.21105/joss.04602)
- 999 Townsend, R. H. D. 2002, MNRAS, 330, 855,
 1000 doi: [10.1046/j.1365-8711.2002.05135.x](https://doi.org/10.1046/j.1365-8711.2002.05135.x)
- 1001 —. 2003, MNRAS, 343, 125,
 1002 doi: [10.1046/j.1365-8711.2003.06640.x](https://doi.org/10.1046/j.1365-8711.2003.06640.x)
- 1003 Townsend, R. H. D., Goldstein, J., & Zweibel, E. G. 2018,
 1004 MNRAS, 475, 879, doi: [10.1093/mnras/stx3142](https://doi.org/10.1093/mnras/stx3142)
- 1005 Townsend, R. H. D., & Teitler, S. A. 2013, MNRAS, 435,
 1006 3406, doi: [10.1093/mnras/stt1533](https://doi.org/10.1093/mnras/stt1533)
- 1007 Vasil, G. M., Julien, K., & Featherstone, N. A. 2021,
 1008 Proceedings of the National Academy of Science, 118,
 1009 e2022518118, doi: [10.1073/pnas.2022518118](https://doi.org/10.1073/pnas.2022518118)
- 1010 Vasil, G. M., Lecoanet, D., Burns, K. J., Oishi, J. S., &
 1011 Brown, B. P. 2019, Journal of Computational Physics: X,
 1012 3, 100013,
 1013 doi: <https://doi.org/10.1016/j.jcpx.2019.100013>
- 1014 Wang, D., & Ruuth, S. J. 2008, Journal of Computational
 1015 Mathematics, 26, 838.
 1016 <http://www.jstor.org/stable/43693484>